minerals

MDPI

Article

Depositional Environments and Carbonaceous Sources of the Cheng-Gang Crystalline Graphite Deposit Revealed by Elemental and Isotopic Evidence

Feng Liu [1], Wenbo Rao [2,*], Yangyang Zhang [1], Jianjun Cui [3] and Weijun Yao [1]

[1] Geological Exploration Technology Institute of Jiangsu Province, Nanjing 210049, China; liufeng015052@163.com (F.L.); zhangyoungyoung@yeah.net (Y.Z.); ywj6228303@163.com (W.Y.)
[2] School of Earth Sciences and Engineering, Hohai University, Nanjing 211100, China
[3] Institute of Geomechanics, Chinese Academy of Geological Sciences, Beijing 100081, China; cagscjj@126.com
* Correspondence: raowenbo@163.com

Abstract

The Cheng-gang crystalline graphite deposit is a recently discovered medium-to-large-sized deposit within the Tan-Lu Fault Zone (TLFZ), East China. However, the knowledge on this deposit remains limited, resulting in a poor understanding of its genesis. In this study, this deposit is chosen to elucidate the degree of graphite mineralization, the nature and depositional environments of the protoliths, and the carbon source of graphite through geochemical and stable isotope investigations, and mineralogical analysis. The fixed carbon contents in the graphite-ore-bearing layers range from 2% to 3%. X-ray diffraction analyses reveal a high degree of graphitization. Analyses of elemental ratios indicate that the protoliths of metamorphic rocks predominantly consist of felsic rocks derived from the upper crust and deposited in brackish-water and reducing environments (anoxic to dysoxic). Stable carbon isotope analyses show that CH_4 with lighter carbon isotopes released from the decomposition of pristine organic matter was trapped into adjacent inorganic reservoirs and the residual fraction with heavy carbon isotopes evolved to become graphite under metamorphism. Assuming the existence of isotope exchange between carbonate minerals and graphite, the temperature of peak metamorphism is estimated to be 580–860 °C, corresponding to amphibolite–granulite facies during regional metamorphism. The direct mixing of organic fluids and adjacent inorganic reservoirs may have contributed to graphite ore formation and needs to be further explored in future studies. The findings shed light on the genesis of the TLFZ graphite deposits, providing practical implications for local mineral exploration.

Keywords: Tan-Lu Fault Zone; graphite deposit; elemental features; stable carbon isotopes; protoliths; depositional environments; carbon source

Check for updates

Academic Editor: Glenn Stracher

Received: 20 November 2025
Revised: 8 January 2026
Accepted: 20 January 2026
Published: 23 January 2026

Copyright: © 2026 by the authors. Licensee MDPI, Basel, Switzerland. This article is an open access article distributed under the terms and conditions of the Creative Commons Attribution (CC BY) license.

1. Introduction

Crystalline graphite, a main type of natural graphite, is characterized by high crystallinity, excellent electrical conductivity, high-refractory proprieties, and chemical stability. Due to these properties, it has found broad applications in key industries, such as renewable energy and nuclear factories. With the rapid increase in the demand driven by emerging technologies, crystalline graphite deposits have been classified as strategic mineral resources in countries such as China and the United States [1,2]. Consequently,

key topics such as depositional environments, carbon sources, and mineralization mechanisms of graphite deposits have increasingly attracted attention in geological sciences worldwide [3–9]. These are still topics of concern to a large extent at present due to the ore-forming model differences in graphite deposits in different geological settings [7,10,11].

Crystalline graphite deposits occur primarily in countries such as China, Brazil, India, Sri Lanka, and Canada [10,12–15]. Their genesis is mainly attributed to two principal processes: regional metamorphism and magmatic–hydrothermal activity. Within regionally metamorphosed deposits, graphite typically occurs as high-crystallinity flakes and is commonly hosted in medium-to-high-grade metamorphic rock series. In this deposit type, graphite forms through the transformation of organic matter under metamorphic conditions; hence, it is characterized by a negative $\delta^{13}C$ value [10,15]. Deposits of magmatic–hydrothermal origin are commonly characterized by lumpy, vein-like, or disseminated graphite with well-developed crystal shapes [3,14–18]. In these types of deposits, graphite develops through the precipitation of carbon-supersaturated C-H-O fluids under certain temperature, pressure and oxygen fugacity conditions, showing more positive $\delta^{13}C$ values [1,4]. China is home to abundant graphite resources, where crystalline graphite deposits mainly cluster within distinct tectonic domains: the North China Craton (e.g., Inner Mongolia, Shandong), the Yangtze Block (e.g., Hubei, Sichuan), and the South China Orogenic Belt (e.g., Fujian, Hunan) [18–23]. Notable examples include deposits in Jixi (Heilongjiang), Nanshu (Shandong), and Nanjiang (Sichuan), primarily linked to regional metamorphism. Extensive research within China, drawing from mineralogical, geochemical, and geochronological perspectives, reveals the main characteristics of regionally metamorphosed crystalline graphite deposits. These may be resumed as follows: (1) protoliths formed in epicontinental shallow marine or back-arc basin environments near continental margins; (2) the deposits predominantly developed in the Proterozoic period in the North China Block but generally younger elsewhere; and (3) the carbonaceous material was derived from organic sources with minor inorganic contributions, and the metamorphism degree varies significantly among regions [12,22–27]. Previous findings give deep insights into the mineralization theory of crystalline graphite deposits and provide important foundations for future research.

Located south of Xinyi in Jiangsu Province, the Cheng-gang crystalline graphite deposit represents a newly discovered medium-sized large-flake crystalline graphite deposit within the Tan-Lu Fault Zone (TLFZ), which is a major Meso-Cenozoic magmatic and tectonic belt in East China [28–30]. Tectonically, this deposit lies in the southeastern edge of the North China Block. Supported by the Natural Resources Development Special Fund of Jiangsu Province, the Jiangsu Geological Exploration Technology Institute has conducted the first detailed exploration on this deposit. Building on this work, Yao et al. (2024) systematically summarized the deposit's geological characteristics, genesis, and prospecting indicators [31], providing pivotal guidance for regional graphite metallogeny and exploration. However, key questions concerning the formation mechanism of crystalline graphite deposits within the TLFZ, as well as their distinctiveness compared to deposits in the North China Block and other regions, remain unresolved. This limits a deep understanding of mineralization processes and hampers precise exploration targeting within this fault zone.

At present, the Cheng-gang crystalline graphite deposit is under exploration. In this study, we focused on this deposit to investigate the mineral composition, elemental geochemistry and stable carbon isotopes. The objectives were to constrain the nature and depositional environment of the protolith and to determine the graphite carbon source. The results are expected to provide deep insights into the genesis of crystalline graphite deposits within the TLFZ and offer practical guidance for exploring similar deposit types.

2. Geological Setting

2.1. Regional Geology

The Cheng-gang crystalline graphite deposit is situated in southern Xinyi City, Jiangsu Province. Tectonically, it lies within the Tan-Lu Fault Zone (TLFZ) along the southeastern margin of the North China Craton (NCC) and is adjacent to the Sulu Orogen Belt (Figure 1a,b). As the largest lithospheric-scale fault zone in eastern China, the TLFZ transects the Yangtze Craton, Dabie-Sulu Orogenic Belt, North China Craton, and Xingmeng Orogenic Belt, comprising numerous secondary fault systems [28–30].

The TLFZ evolution experienced multiple tectono-thermal stages. During the Precambrian basement metamorphism stage (Neoarchean to Paleoproterozoic), the TLFZ underwent high-temperature metamorphism (500–700 °C) with the development of amphibolite-to-granulite-facies gneisses and granulite, which was associated with early deep crustal thermal events in the North China Craton [32]. During the collision between the Yangtze Plate and North China Plate, syn-collisional metamorphism occurred at moderate temperatures (300–500 °C), generating greenschist-to-lower-amphibolite facies metamorphic rocks within this fault zone.

During the Middle to Late Mesozoic period (approximately 160–90 Ma B.P.), due to the subduction of the Pacific Plate, the TLFZ experienced sinistral strike-slip motion accompanied by intense magmatic intrusions, locally reaching temperatures up to 600 °C. During the Cenozoic period (Himalayan period), the TLFZ was dominated by dextral strike-slip and extensional activities, with a significant decrease in metamorphic temperature (200–400 °C). This manifested as low-temperature greenschist facies metamorphism and brittle–ductile deformation, locally influenced by Cenozoic basalt eruptions [33].

The timing of major strike-slip activity within the TLFZ, interpreted from mylonite ages and basin evolution, remains debated: authors proposed Late Jurassic–Early Cretaceous, Early Cretaceous, or Triassic or Middle Triassic–Jurassic [28–30,32–35]. Despite the discrepancies, a broad consensus identifies the TLFZ as a major Mesozoic lithospheric thinning zone, with its peak magmatic activity contemporaneous with widespread events across the North China region [36].

2.2. Geology of Study Area

The strata in the study area include the Cheng-gang Rock Group (the Neoarchean to Paleoproterozoic), the Wangshi Formation of the Late Cretaceous, the Suqian Formation of the Pliocene, and the Quaternary System (Figure 1c). The Cheng-gang Rock Group is a medium-to-high-grade metamorphic rock series. Its upper part consists of gneiss formations, mainly composed of plagioclase gneiss interbedded with granite gneiss. Its middle part, which is the graphite ore-hosting layer, consists of amphibolite–plagioclase gneiss interbedded with graphite-bearing plagioclase gneiss and marble. Its lower part comprises magnetite-bearing metamorphic rocks, consisting of magnetite-bearing biotite plagioclase gneiss and granite gneiss. The Wangshi Formation is composed of conglomerate, medium-to-fine-grained sandstone, and silty shale. The Suqian Formation consists of grayish-white, medium-to-coarse-grained sand and gravelly medium-to-coarse-grained sand. The Quaternary System is widely distributed within the area, characterized by sand-gravel layers, gravelly sub-clay, and calcareous nodule-bearing sub-clay. The latter two strata overlie the former two strata, which are not displayed in Figure 1c.

The study area is structurally dominated by a set of NNE-SSW trending faults belonging to the major and secondary systems within the TLFZ (Figure 1b,c). The magmatic rocks in the study area are primarily Neoarchean to Paleoproterozoic mafic and ultramafic rocks, along with Mesozoic granites.

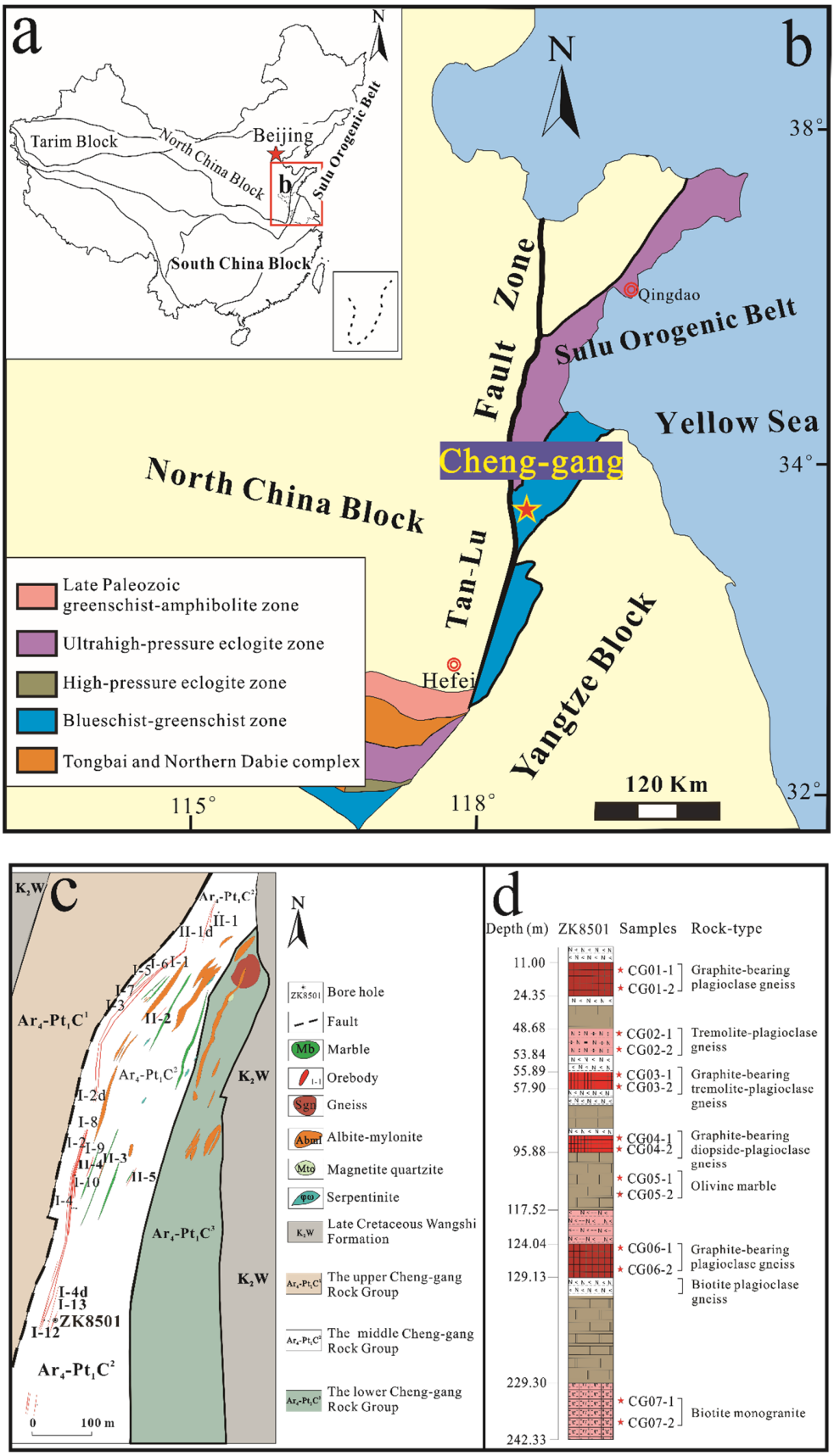


Figure 1. Map showing the location of the study area (**a**), regional geology (**b**), geology of the ore district (**c**), drilling profile location and sampling (**d**). Red star denotes sampling location in subfigure (**d**).

Metamorphic rocks in the study area include various gneisses, marbles, and amphibolites with a tiny number of serpentinites. These rocks underwent medium-pressure amphibolite facies metamorphism during the Paleoproterozoic period, with primary metamorphic minerals such as glaucophane (bluish-green amphibole), biotite, and diopside. Subsequently, these rocks were overprinted by low- or medium-pressure greenschist facies metamorphisms during the Mesozoic period, characterized by metamorphic minerals such as chlorite, serpentine, and albite.

Graphite mineralization occurred within the middle part of the Cheng-gang Rock Group (Figure 1c). Based on the occurrence positions, strikes, and host layers, two graphite mineralized areas have been delineated: Zone I and Zone II. Within Zone 1, the principal ore bodies were designated I-1, I-2, I-3, and I-4. The graphite mineralized zone II is located east of zone I. Overall, the ore is a flake graphite gneiss.

3. Sampling Activity

A field campaign was conducted in December 2024 to collect core samples from layers CG01 to CG07 in borehole ZK8501 within the study area (Figure 1d). Two samples were collected from the top and bottom of each layer, totaling 14 samples (Figure 1d). CG01, CG03, CG04, and CG06 are the four graphite-ore-bearing layers, located at depths of 11–24 m, 55–59 m, 90–95 m, and 124–129 m, respectively. Their lithologies are graphite-bearing plagioclase gneiss, graphite-bearing tremolite–plagioclase gneiss, graphite-bearing diopside–plagioclase gneiss, and graphite-bearing plagioclase gneiss, respectively. Graphite, identified as the ore mineral, appears black with a lead-gray streak and predominantly occurs in flaky or foliated forms.

CG02 is located at a depth of 48–54 m, with the lithology consisting of tremolite–plagioclase gneiss. It is gray-black to gray, exhibiting a lepidoblastic texture and a gneissic structure. The mineralogy comprises plagioclase, quartz, tremolite, and biotite. CG05, located at a depth of 95–118 m, consists of olivine marble displaying gray-white to dark green colors. It exhibits a granoblastic texture and a massive structure, with main minerals consisting of calcite, olivine, and phlogopite. CG07 is located at a depth of 186–242 m, with the lithology consisting of gray-white biotite monzogranite. The mineralogy mainly consists of plagioclase, quartz, amphibole, K-feldspar, and minor biotite.

4. Analytical Methods

4.1. Sample Preparation

All samples were ground to <63 μm using an agate mortar prior to the analysis of fixed carbon and elemental contents, as well as stable carbon isotopes of carbonates. Eight samples collected from four graphite-ore-bearing layers were subjected to acid digestion using 2M HCl solution to eliminate inorganic carbon prior to graphite carbon isotope analysis. Two samples from the upper and bottom portions of each layer were pooled and ground to <63 μm using for whole-rock X-ray diffraction (XRD) analysis. Additionally, for layers CG01, CG03, and CG06, two samples from each respective layer were mixed and crushed to manually pick out as much graphite as possible via a binocular microscope. The obtained graphite samples were ground to <63 μm for graphite XRD analysis. The sample preparation was conducted at the Geochemical Laboratory of Hohai University.

4.2. Fixed Carbon Analysis

The powder samples were digested with dilute hydrochloric acid to remove inorganic carbon. Then, the digested sample was burnt at approximately 500 °C to get rid of organic carbon. Finally, the residue was analyzed at about 1100 °C for fixed carbon content using an elemental analyzer (Vario EL cube, Elementar, Frankfurt, Germany) with a relative error

of 5% [22]. The analyses were carried out at the School of Earth Sciences and Engineering, Nanjing University.

4.3. X-Ray Diffraction (XRD) Analysis

The XRD analysis of samples was performed for mineral characterization by using a X-ray diffractometer (DX-2700, Haoyuan Instrument, Dandong, China) at the School of Earth Sciences and Engineering, Hohai University. The instrument operating conditions were 30 KV voltage at 20 mA current with a CuKα radiation. The analyses were acquired at a step size of 0.02°, from 5° to 80° (2θ), using a scanning speed of 2°/min, and an X-ray wavelength of 0.15406 nm. The X-ray diffraction patterns were subjected to smoothing, background stripping, and background subtraction using Jade 6.5 software. The graphitization degree (r) was calculated using the following formula

$$r = (0.3440 - d002)/(0.3440 - 0.3354) \times 100\% \quad (1)$$

where d002 is the main peak of graphite [37].

4.4. Chemical Analysis

Approximately 0.6 g of powdered sample in a platinum crucible was ignited at approximately 1000 °C for 3 h to determine the loss on ignition (LOI). After adding 6.6 g of a lithium tetraborate–lithium metaborate flux mixture and 0.6 mL of lithium bromide solution (40 mg/mL) to the crucible, the sample was fused at temperatures exceeding >1000 °C to produce a glass bead. The resulting bead was analyzed using a X-ray Fluorescence Spectrometer (ARL9800XP+, Thermo Fisher Scientific Inc., Waltham, MA, USA) at the Center of Modern Analyses, Nanjing University. Calibration was performed using national geological reference materials (Appendix A, Tables A1–A3), with relative errors of 10% for MgO, Na_2O, P_2O_5, and MnO, and 5% for other oxides.

For minor, trace and rare earth element analyses, 50 mg of the powdered sample was weighed into a polytetrafluoroethylene (Teflon) digestion vessel, digested with a 1:4 HNO_3-HF mixed acid at 190 °C for 72 h, then evaporated to dryness. After dissolving the residue with 3 mL of 2 mol/L HNO_3, the solution was diluted to a constant volume with a 2% HNO_3 solution and analyzed using an ICP-Q Inductively Coupled Plasma Mass Spectrometer (Thermo Fisher Scientific Inc., USA) at Nanjing Institute of Geology and Palaeontology, Chinese Academy of Sciences. National geological reference materials (Appendix A, Tables A1–A3) were also used as analytical standards, with deviations below 5% between measured and certified reference values.

4.5. Stable Carbon Isotope Analysis

The stable carbon isotope composition of graphite was determined using an elemental analyzer (EA3000, EuroVector, Pavia, Italy) coupled with a continuous-flow isotope ratio mass spectrometer (IsoPrime GV instruments, Elementar, Manchester, UK) at Guiyang Institute of Geochemistry, Chinese Academy of Sciences. The carbon powder reference materials employed were GBW04407 ($\delta^{13}C_{VPDB}$ = −22.43‰) and GBW04408 (δ^{13}CVPDB = −36.91‰).

Carbon dioxide was collected from the carbonate dissolution of the sample by adding enough phosphoric acid (100%), purified via vacuum extraction, and introduction to a gas isotope ratio mass spectrometer (MAT252, Finnigan MAT/Thermo Fisher, Bremen, Germany) for five replicate measurements in dual-inlet mode. The isotopic reference standards used were NBS19 ($\delta^{13}C_{VPDB}$ = +1.95‰), GBW04405 ($\delta^{13}C_{VPDB}$ = +0.57‰), and GBW04406 ($\delta^{13}C_{VPDB}$ = −10.85‰).

The $\delta^{13}C$ values for both graphite and carbonate were reported on the [‰ VPDB-Vienna Pee Dee Belemnite] scale as defined by the following equation [38], with analytical precisions better than 0.15‰ and 0.05‰, respectively,

$$\delta^{13}C_{sample}\ (‰) = [(^{13}C/^{12}C_{sample})/(^{13}C/^{12}C_{VPDB}) - 1] \times 1000 \quad (2)$$

5. Results

5.1. Mineralogy

The mineral assemblages of major rocks in the Cheng-gang crystalline graphite deposit are displayed in Figure 2. The gneiss contains graphite, quartz, plagioclase, tremolite, and hornblende. The marble primarily consists of calcite with minor amounts of olivine and phlogopite, and the granite is dominated by quartz and hornblende with subordinate olivine and phlogopite. The mineral composition in the gneiss varies across different layers (Figure 2). According to the XRD results (Figure 2) and fixed carbon contents described in the following Section 5.5, together with hand specimens, within the graphite-ore-bearing layers (CG01, CG03, CG04, CG06), the main minerals include quartz, plagioclase, and hornblende, with the minor mineral (olivine) and the ore mineral (graphite). In contrast, in layer CG02, quartz and plagioclase are the main minerals, accompanied by minor minerals such as tremolite and biotite. The XRD analysis reveals d002 peaks of graphite in layers CG01, CG03, and CG06, the same as quartz (Figure 2). The main peaks of graphite minerals are sharp and well-defined, with interlayer spacings of 3.3811 Å, 3.3810 Å, and 3.3805 Å, respectively, for the three layers. The interlayer spacings approach the range of semi-graphite [39], but the calculated r values for these three layers are 0.68488, 0.68605, and 0.69186, respectively, implying a high degree of graphitization in this deposit. So, the XRD result of graphite needs to be further verified in the future.

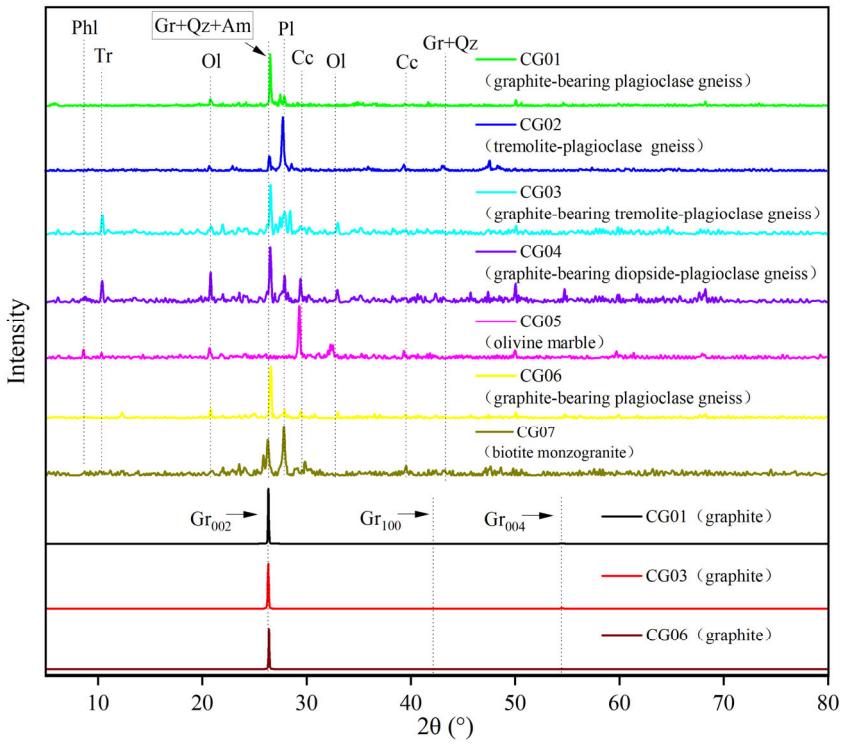


Figure 2. The X-ray diffraction spectra of the whole-rock and graphite samples from the Cheng-gang crystalline graphite deposit. Am—amphibole, Cc—calcite, Gr—graphite, Ol—olivine, Phl—phlogopite, Pl—plagioclase, Qz—quartz, Tr—tremolite.

5.2. Major Elements

The major element data of bulk rock samples from borehole ZK8501 are listed in Table 1 and displayed in Figure 3. The SiO_2 content exceeds 35.83% in all samples, higher than other element contents within each layer, yet lower than values typical of the Upper Continental Crust (UCC) and the Post-Archean Australian Shale (PAAS) [40,41]. The SiO_2 contents are higher in all layers, except the marble layer (CG05-1 and CG05-2), than the primitive mantle (PM) value [42]. The CaO contents are variable from one layer to another with an average of 13.56%, which is higher than the UCC, PAAS and PM values [40–42]. On average, the Al_2O_3 content is 11.59%, slightly below the CaO content, and falls below the UCC and PAAS values but exceeds the PM value [40–42]. The contents of other elements are, on average, below 10%, of which the average contents of Fe_2O_3, FeO, MgO, Na_2O, K_2O, and LOI are between 1% and 10%, while the contents of MnO, P_2O_5 and TiO_2 average less than 1%.

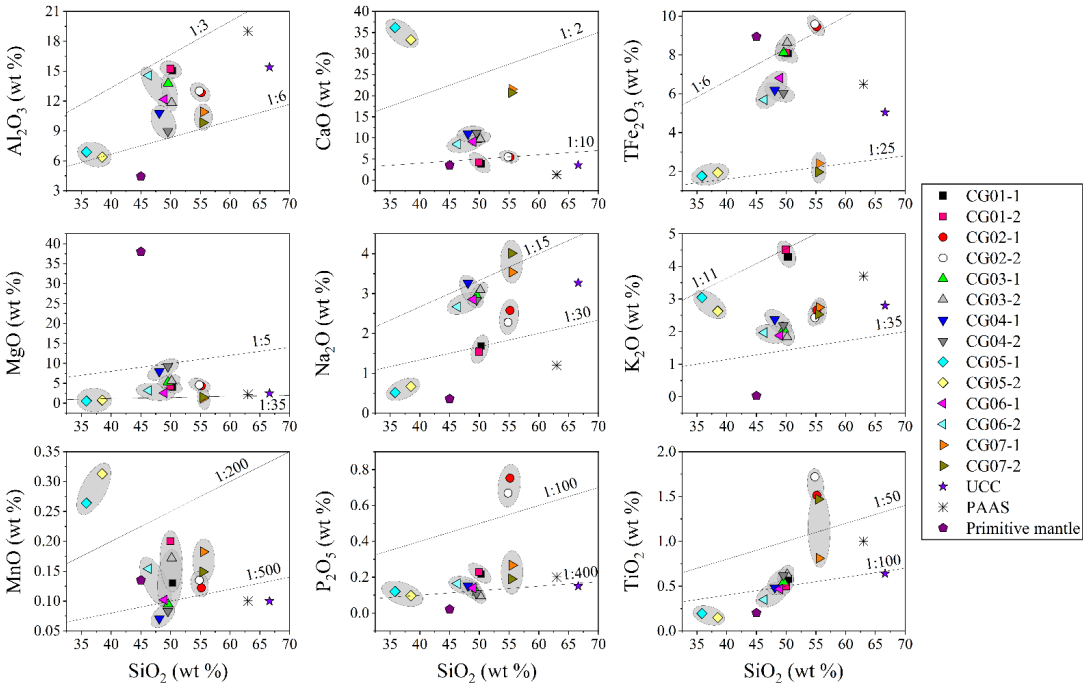


Figure 3. Scatter plots showing the relationships between silicon and other major elements in rock samples from the Cheng-gang crystalline graphite deposit. The UCC, PAAS and primitive mantle data are from references [40–42]. Gray color covers the two samples from the same layer.

The contents of major elements show minimal variations between samples within the same layer but exhibit substantial variations across layers (Figure 3). In particular, the contents of SiO_2, Al_2O_3, TFe_2O_3, MgO, Na_2O, and TiO_2 are the lowest in CG05 (marble), coupled with the highest contents of CaO, MnO and LOI. The highest SiO_2 and Na_2O contents and the lowest LOI and FeO contents are for CG07 (biotite monzogranite). There are the highest contents of Al_2O_3, K_2O, and Fe_2O_3 and the lowest FeO content in CG01; the highest contents of TFe_2O_3, P_2O_5, and TiO_2 in CG02; the highest MgO and FeO contents and the lowest MnO and Fe_2O_3 contents in CG04; and the highest LOI contents and the lowest K_2O content in CG06. The SiO_2/Al_2O_3 ratio varies significantly from 3.18 to 6.04 across rock layers, reaching its maximum in CG05-2 and minimum in CG06-2 (Table 1). The K_2O/Na_2O ratio exceeds 1 in the layers CG01, CG02, and CG05 but drops below 1 in other layers, fluctuating between 0.59 and 5.9 (Table 1). The Al_2O_3/TiO_2 ratio changes between 6.69 and 42.75 across rock layers, with the maximum in CG05-2 and the minimum in CG07-2 (Table 1).

Table 1. Contents and typical parameters of major, minor, trace and rare earth elements in rocks from the Cheng-gang crystalline graphite deposit.

Sample	CG01-1	CG01-2	CG02-1	CG02-2	CG03-1	CG03-2	CG04-1	CG04-2	CG05-1	CG05-2	CG06-1	CG06-2	CG07-1	CG07-2
Depth/m	**11–18**	**18–24**	**48–51**	**51–54**	**55–57**	**57–59**	**90–92**	**92–95**	**95–106**	**106–118**	**124–127**	**127–129**	**186–209**	**209–242**
Rock Type	**Graphite-Bearing Plagioclase Gneiss**		**Tremolite–Plagioclase Gneiss**		**Graphite-Bearing Tremolite–Plagioclase Gneiss**		**Graphite-Bearing Diopside–Plagioclase Gneiss**		**Olivine Marble**		**Graphite-Bearing Plagioclase Gneiss**		**Biotite Monogranite**	
SiO_2	50.30	49.95	55.15	54.83	49.57	50.16	48.09	49.53	35.83	38.49	48.96	46.31	55.51	55.41
Al_2O_3	15.03	15.23	12.83	13.01	13.78	11.83	10.80	8.96	6.88	6.37	12.16	14.57	10.91	9.83
TFe_2O_3	8.07	8.12	9.45	9.59	8.12	8.64	6.18	6.04	1.75	1.93	6.81	5.69	2.40	1.96
MgO	3.98	4.18	4.32	4.57	5.31	5.57	7.94	9.18	0.55	0.76	2.55	3.18	1.19	1.48
CaO	3.87	4.23	5.43	5.51	9.61	9.72	10.96	11.21	36.16	33.24	9.14	8.51	21.54	20.73
Na_2O	1.69	1.54	2.58	2.28	2.95	3.09	3.26	2.84	0.52	0.67	2.85	2.67	3.54	4.01
K_2O	4.29	4.51	2.66	2.43	2.07	1.83	2.38	2.19	3.04	2.63	1.88	1.97	2.75	2.53
MnO	0.13	0.20	0.12	0.14	0.09	0.17	0.07	0.08	0.26	0.31	0.10	0.15	0.18	0.15
P_2O_5	0.22	0.23	0.75	0.67	0.11	0.10	0.15	0.11	0.12	0.10	0.14	0.16	0.27	0.19
TiO_2	0.58	0.50	1.51	1.72	0.55	0.63	0.48	0.62	0.19	0.15	0.47	0.35	0.81	1.47
LOI	11.65	10.89	4.66	3.98	9.75	8.96	9.54	8.34	15.12	13.73	14.84	15.46	1.19	1.37
FeO	0.29	0.31	2.17	2.24	2.87	2.55	5.06	4.99	0.62	0.77	4.48	4.36	0.42	0.38
ΣM	99.80	99.58	99.48	98.72	101.91	100.70	99.85	99.10	100.43	98.38	99.90	99.03	100.29	99.13
SiO_2/Al_2O_3	3.35	3.28	4.30	4.21	3.60	4.24	4.45	5.53	5.21	6.04	4.02	3.18	5.09	5.64
K_2O/Na_2O	2.55	2.93	1.03	1.07	0.70	0.59	0.73	0.77	5.90	3.93	0.66	0.74	0.78	0.63
Al_2O_3/TiO_2	25.92	30.64	8.48	7.57	25.2	18.75	22.37	14.47	35.35	42.75	26.00	41.75	13.46	6.69
Li	34.00	36.45	21.64	24.52	22.05	21.68	21.95	20.17	22.05	19.84	50.87	44.62	4.95	7.13
Rb	115.20	106.00	105.46	111.61	54.12	49.36	84.69	80.91	52.97	48.37	48.57	49.64	43.01	42.99
Cs	2.50	2.27	5.18	5.63	0.58	0.50	2.32	3.06	1.69	1.77	2.71	2.65	0.58	0.64
Sr	232.30	198.00	276.92	318.87	185.32	180.64	323.50	297.00	248.37	245.27	177.50	193.00	187.79	200.70
Ba	899.10	905.00	454.45	461.61	550.61	534.58	599.50	573.00	1702.00	1698.58	469.50	461.00	603.19	595.08
Sc	17.51	19.11	13.75	13.88	15.80	12.64	25.75	26.19	24.12	22.12	21.70	19.33	27.69	23.57
V	194.20	165.00	68.33	67.32	109.06	102.64	192.00	206.00	123.55	134.65	190.70	173.00	55.22	49.14
Cr	44.32	39.15	29.03	23.65	93.49	88.72	42.92	45.11	74.42	68.04	33.16	39.46	8.34	6.31
Co	29.39	23.64	6.54	7.17	20.75	17.30	23.06	20.20	23.88	18.95	30.23	27.50	10.46	12.04
Ni	97.64	88.60	20.53	19.93	48.27	44.16	59.53	51.34	34.58	39.16	70.70	66.40	7.05	7.94
Cu	94.74	88.31	12.86	13.41	105.02	100.39	63.82	59.12	38.05	33.20	148.10	129.00	3.13	3.34
Zn	247.00	268.00	162.28	150.14	67.05	59.36	212.60	198.00	131.16	163.72	155.00	121.74	6.24	5.70
Zr	165.40	113.50	237.34	225.44	275.89	301.77	123.40	118.00	236.97	219.47	94.56	85.39	47.00	42.97
Nb	12.52	11.60	7.63	6.98	6.18	6.62	7.48	7.11	8.57	8.01	10.31	10.80	20.63	19.91
Hf	5.03	4.81	5.42	4.90	6.38	6.28	3.58	3.67	5.40	5.52	2.78	2.59	1.06	1.01

Table 1. *Cont.*

Sample	CG01-1	CG01-2	CG02-1	CG02-2	CG03-1	CG03-2	CG04-1	CG04-2	CG05-1	CG05-2	CG06-1	CG06-2	CG07-1	CG07-2
Depth/m	**11–18**	**18–24**	**48–51**	**51–54**	**55–57**	**57–59**	**90–92**	**92–95**	**95–106**	**106–118**	**124–127**	**127–129**	**186–209**	**209–242**
Rock Type	**Graphite-Bearing Plagioclase Gneiss**		**Tremolite–Plagioclase Gneiss**		**Graphite-Bearing Tremolite–Plagioclase Gneiss**		**Graphite-Bearing Diopside–Plagioclase Gneiss**		**Olivine Marble**		**Graphite-Bearing Plagioclase Gneiss**		**Biotite Monogranite**	
Ta	1.08	1.05	0.66	0.50	0.40	0.42	0.67	0.78	0.40	0.41	0.81	0.69	0.95	0.87
Pb	108.30	116.00	226.46	221.99	8.97	7.90	32.68	29.82	25.26	26.11	413.90	397.00	7.89	8.14
Th	14.62	16.10	8.99	8.65	3.98	3.75	6.80	6.98	4.66	4.20	2.61	2.17	7.33	6.79
U	3.97	3.84	3.72	4.16	1.47	1.37	4.40	3.97	1.25	1.19	1.05	1.19	0.90	0.89
Y	39.46	37.46	35.31	35.82	29.37	27.48	22.90	21.50	20.42	20.14	19.38	17.90	40.35	39.12
Cr/Zr	0.27	0.34	0.12	0.10	0.34	0.29	0.35	0.38	0.31	0.31	0.35	0.46	0.18	0.15
Sr/Ba	0.26	0.22	0.61	0.69	0.34	0.34	0.54	0.52	0.15	0.14	0.38	0.42	0.31	0.34
Th/U	3.69	4.19	2.41	2.08	2.70	2.75	1.55	1.76	3.73	3.52	2.49	1.82	8.13	7.62
V/(Ni + V)	0.67	0.65	0.77	0.77	0.69	0.70	0.76	0.80	0.78	0.77	0.73	0.72	0.89	0.86
&U	0.90	0.83	1.11	1.18	1.05	1.04	1.32	1.26	0.89	0.92	1.09	1.24	0.54	0.56
La	58.42	53.80	58.67	54.98	29.30	27.64	32.45	29.74	67.77	68.82	23.95	22.42	85.99	81.65
Ce	109.70	128.00	112.96	109.74	51.02	49.88	56.78	55.70	125.49	119.88	43.38	42.97	146.53	143.15
Pr	11.50	9.97	12.78	11.65	5.72	4.98	6.94	8.11	13.57	12.46	5.52	5.62	14.71	12.67
Nd	42.85	41.88	45.14	43.98	19.88	18.65	26.27	23.90	47.81	47.44	21.41	22.18	49.89	48.95
Sm	7.61	8.02	8.43	8.65	3.51	3.95	4.67	4.92	5.39	5.51	4.14	3.85	8.47	7.64
Eu	1.88	1.97	1.97	2.06	1.22	1.65	1.22	1.34	1.67	1.51	1.33	1.57	2.30	2.19
Gd	7.65	7.43	7.86	8.61	3.01	3.12	4.64	4.51	3.60	4.05	3.93	3.76	8.18	7.92
Tb	1.14	1.09	1.15	1.29	0.41	0.38	0.69	0.57	0.75	0.82	0.63	0.68	1.17	1.09
Dy	6.45	7.56	7.32	7.65	2.55	2.97	3.80	4.01	3.47	3.67	3.44	2.98	6.82	5.84
Ho	1.34	1.24	1.38	1.50	0.52	0.48	0.79	0.69	0.66	0.55	0.70	0.76	1.41	1.39
Er	3.71	3.61	3.79	4.09	1.46	1.37	2.57	2.36	1.70	1.60	2.46	2.94	3.48	3.85
Tm	0.55	0.49	0.55	0.49	0.20	0.16	0.33	0.28	0.21	0.24	0.28	0.31	0.51	0.48
Yb	3.42	3.14	3.61	3.87	1.25	1.17	2.11	2.34	1.33	1.43	1.79	1.90	3.54	3.49
Lu	0.52	0.61	0.56	0.57	0.20	0.20	0.33	0.34	0.19	0.21	0.26	0.28	0.54	0.50
ΣREEs	256.72	268.81	266.14	259.13	120.25	116.59	143.59	138.80	273.64	268.18	113.23	112.20	333.53	320.80
LREE/HREE	9.36	9.68	9.16	8.23	11.52	10.83	8.40	8.19	21.95	20.33	7.39	7.25	12.01	12.06
La/Yb	17.11	17.13	16.27	14.20	23.53	23.67	15.36	12.71	50.82	48.23	13.40	11.80	24.29	23.40
$(La/Yb)_N$	11.40	11.42	10.85	9.47	15.68	15.78	10.24	8.47	33.88	32.15	8.93	7.87	16.19	15.60
δCe	0.97	0.96	0.96	0.90	0.90	0.88	0.88	0.95	0.95	0.88	0.88	0.92	0.92	1.03
δEu	0.70	0.69	0.69	1.06	1.06	0.75	0.75	1.03	1.03	0.94	0.94	0.79	0.79	0.63

Note: The unit is % for the major element content, and μg/g for the trace and rare earth element content. LOI is the loss on ignition. ΣM is the sum of major oxides plus LOI. &U is U/[0.5 + (Th/3 + U]. ΣREEs is the sum of rare earth element contents, LREE/HREE is the ratio of light to heavy rare earth element contents, and $(La/Yb)_N$, δCe, and δEu are the calculated chondrite-normalized values. $\delta Ce = 2 \times Ce_N/(La_N + Pr_N)$, $\delta Eu = 2 \times Eu_N/(Sm_N + Gd_N)$, where N indicates chondrite normalization [41].

5.3. Geochemistry of Minor and Trace Elements

Minor and trace element contents of metamorphic rock samples collected in borehole ZK8501 are listed in Table 1 and shown in Figure 4a. Among the large-ion lithophile elements (LILE), the Ba content is the highest, ranging from 454.45 to 1702 μg/g, followed by the Sr and Rb contents, ranging from 177.5 to 323.5 μg/g and 48.37 to 115.2 μg/g, respectively, and the Li and Cs contents are below 51 μg/g and 6 μg/g, respectively. These element contents vary greatly with layers. For example, there is the highest Li content in CG06, reaching 40–50 μg/g, while the Rb content is higher in CG01 and CG02, exceeding 105 μg/g. Among the transition metal elements (TME), the Zn and V contents are relatively higher, ranging from 59.36 to 268 μg/g and 67.32 to 206 μg/g, respectively, followed by the Cu, Ni, and Cr contents ranging from 12.86 to 148.1 μg/g, 19.93 to 97.64 μg/g, and 23.65 to 93.49 μg/g, respectively. Co and Sc display relatively lower contents, varying between 6.54 and 30.23 μg/g, and between 12.64 and 26.19 μg/g, respectively. The TME contents also change with layers, namely, the V and Sc contents are the highest in CG04, the Cr content is the highest in CG03, the Co and Cu contents are the highest in CG06, and the Ni content is the highest in CG01. The contents of all the TMEs are the lowest in CG02. Among the high field strength elements (HFSE), the Zr and Pb contents are relatively higher, with ranges from 85.39 to 301.77 μg/g and 7.9 to 413.9 μg/g, respectively, and the Nb, Th, and Y contents vary from 6.18 to 12.52 μg/g, from 2.17 to 16.1 μg/g, and from 17.9 to 39.46 μg/g, respectively. Compared to the above-mentioned elements, Hf, Ta, and U display relatively lower contents from 2.59 to 6.38 μg/g, from 0.4 to 1.08 μg/g, and from 1.05 to 4.4 μg/g, respectively. In addition, the Zr, Hf, U, Th, and Y contents are the lowest in CG06, the Pb and Nb contents are the lowest in CG03, and the Ta content is the lowest in CG05, while the Nb, Ta, Th, and Y contents are the highest in CG01, the Zr and Hf contents are the highest in CG03, the Pb content is the highest in CG06, and the U content is the highest in CG04. In addition, it is observed that the contents of minor and trace elements are different to some degree among graphite-ore-bearing layers (CG01, CG03, CG04 and CG06).

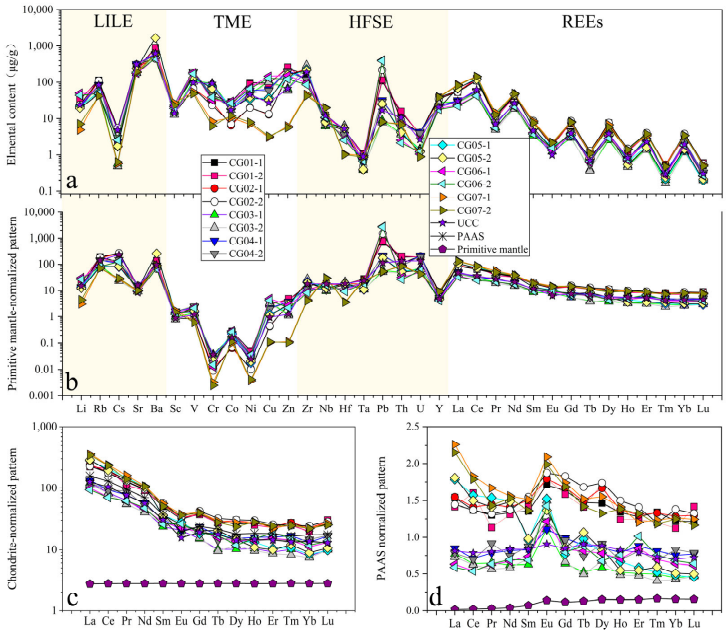


Figure 4. The contents (**a**) and primitive mantle-normalized patterns (**b**) of minor, trace elements and rare earth elements, and the chondrite- (**c**) and PAAS- (**d**) normalized patterns of rare earth elements in samples from the Cheng-gang crystalline graphite deposit. The UCC, PAAS and primitive mantle data are from references [40–42]. LILE means large-ion lithophile element, TME denotes high field strength element, and HFSE is transition metal element.

Compared to the metamorphic rock samples, the granite samples from CG07 show (1) similar LILE ranges except for notably lower Cs (<1 μg/g) and Li (10 μg/g), (2) lower contents of the transition metal elements within the range of 3–56 μg/g, and (3) higher Nb and Y contents (19–21 and 39–41 μg/g, respectively) but lower contents of Zr, Hf, Pb and U (Table 1 and Figure 4a).

The primitive mantle-normalized minor and trace element patterns of all samples from various layers are broadly similar (Figure 5b). Compared to the primitive mantle values [42], all samples show significant enrichment in LILEs and HFSEs, coupled with substantial depletion in TMEs such as Cr, Co, and Ni (Figure 4b).

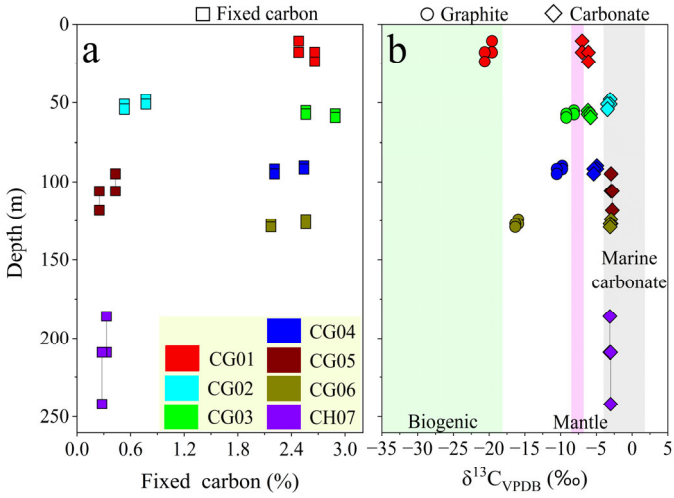


Figure 5. Fixed carbon content (**a**), $\delta^{13}C_{VPDB}$ values (**b**) of graphite and carbonate in samples from the Cheng-gang crystalline graphite deposit. The rock names for various layers are described in Section 3.

5.4. Rare Earth Elements

The total contents of the rare earth elements (REEs) in the metamorphic rock samples range from 112.2 to 273.64 μg/g, showing significant variations across layers, with the lowest value in CG06 and the highest in CG05 (Table 1 and Figure 4a). It is seen that the REE totals of the graphite-ore-bearing layers are variable to some extent, but overall lower than those of other metamorphic rock layers (Table 1 and Figure 4a). The Ce content exceeds 100 μg/g in CG01, CG02, CG05, and CG07, while all other REE contents remain below 100 μg/g (Figure 4a). Moreover, the Lu, Tm, Ho, and Tb contents are typically below 1 μg/g in most samples (Figure 4a).

The chondrite-normalized REE patterns of the metamorphic rock samples across all layers exhibit consistent right-skewed curves, indicating the enrichment of light rare earth elements (LREEs) and the depletion of heavy rare earth elements (HREEs) (Figure 4c). The LREE/HREE, La/Yb, and $(La/Yb)_N$ ratios in these rocks change between 7.25 and 21.95, between 11.8 and 50.8, and between 7.87 and 33.88, respectively (Table 1). All these parameters are the lowest in CG06 but the highest in CG05 (Table 1). In addition, δCe values change minimally from 0.88 to 0.97, whereas δEu values fluctuate more broadly from 0.69 to 1.06 in the metamorphic rock samples, reaching the lowest in CG01 and the highest in CG05 (Table 1).

The total REE contents range from 320 to 334 μg/g in the graphite samples from CG07, significantly higher than the values in the overlying metamorphic rock layers (Table 1). Despite this, the chondrite-normalized REE pattern of this layer was similar, with LREE/HREE, La/Yb, and $(La/Yb)_N$ ratios lying within the range of the metamorphic rock samples and indicating persistent LREE enrichment and HREE depletion (Figure 4c). In

contrast, the δCe values of this layer are slightly higher, with a range of 0.92 to 1.03, while δEu values are lower, with a range between 0.63 and 0.79 (Table 1).

As illustrated in Figure 4a,d, REEs in layers CG01, CG02, CG05, and CG07 are relatively enriched compared to the PAAS values, whereas those in other layers are depleted, which needs to be further explored in future studies. The PAAS-normalized patterns of REEs differ significantly with layers, but they all exhibit distinct positive Eu anomalies (Figure 4d). These patterns can be broadly classified into three categories (Figure 4d). The first one is that samples from CG05 are characterized by the right-leaning PAAS-normalized REE patterns with LREE enrichment, HREE depletion, and abnormal Sm and Tb behaviors. The second one is that samples from CG07 show the right leaning of the PAAS-normalized LREE and HREE patterns. The last one is that samples from the remaining layers display the PAAS-normalized REE pattern with a flat LREE segment and a right-leaning HREE segment. The PAAS-normalized REE distribution patterns of all samples differ markedly from those of UCC and primitive mantle (Figure 4d).

5.5. Fixed Carbon Content and Stable Carbon Isotope Compositions

The fixed carbon contents in host-rock samples from various layers of borehole ZK8501 are listed in the Supplementary Material (Table S1) and displayed in Figure 5a. The fixed carbon contents of all samples range from 0.28% to 2.89%, usually higher in the graphite-ore-bearing layers as expected, with 2.48%–2.66%, 2.56%–2.89%, 2.21%–2.54%, and 2.17%–2.56% in layers CG01, CG03, CG04 and CG06, respectively, but below 1% in other layers (Figure 5a).

The $\delta^{13}C_{VPDB}$ value of graphite, varying from −8.13‰ to −20.61‰, is the most negative in CG01 (~−20.1‰), plotting within the biogenic field, whereas samples from CG03 display more positive $\delta^{13}C_{VPDB}$ values (~−8.67‰), trending toward the mantle and marine carbonate fields but closer to the mantle field (Figure 5b). The $\delta^{13}C_{VPDB}$ value of graphite in CG04 is similar to that in CG03, while it is more negative (~−16.13‰) in CG06, plotting between organic and inorganic fields (Figure 5b).

The $\delta^{13}C_{VPDB}$ values of carbonates in all samples from various layers vary from −2.76‰ to −6.99‰ with a mean value of –4.21‰, slightly increasing with depth (Figure 5b). The $\delta^{13}C_{VPDB}$ values of carbonates from most layers plot within the marine carbonate field, but the $\delta^{13}C_{VPDB}$ values from layers CG01, CG03, and CG04 fall between the organic and marine carbonate fields, closer to the mantle and marine carbonate fields (Figure 5b).

6. Discussion

6.1. The Nature of the Original Rock

Some elements such as Ti, Zr and Hf have relatively stable geochemical behaviors and may effectively avoid the interference from mobile components (e.g., H_2O, CO_2, K_2O, and Na_2O) during metamorphism; thus, their discrimination diagrams provide reliable results for understanding the protoliths of metamorphic rocks [43–46]. As shown in Figure 6a, the metamorphic rock samples plot within the sedimentary rock field, indicating a para-metamorphic rock type (sedimentary protolith). Samples from layer CG07 fall within the igneous rock field, confirming its magmatic origin. The plot of La/Yb vs. ΣREEs (Figure 6b) shows that most of the metamorphic rock samples are located within sedimentary rock fields, particularly argillaceous sedimentary rocks such as calcareous mudstones, while a few overlapped with magmatic rock areas. This corroborates that the protoliths of metamorphic rocks in most layers have a sedimentary origin, whereas rock samples from layer CG07 are of magmatic origin. Additionally, in Figure 6c, most samples plot within the quartzite field, while samples from CG01 are located within the field of basic volcanic rocks or dolomitic mudstone, and samples from CG05 fall within the field of calcareous

carbonate rocks. These findings collectively demonstrate the protoliths of metamorphic rocks dominated by greywacke, felsic clastic rocks, and carbonate rocks.

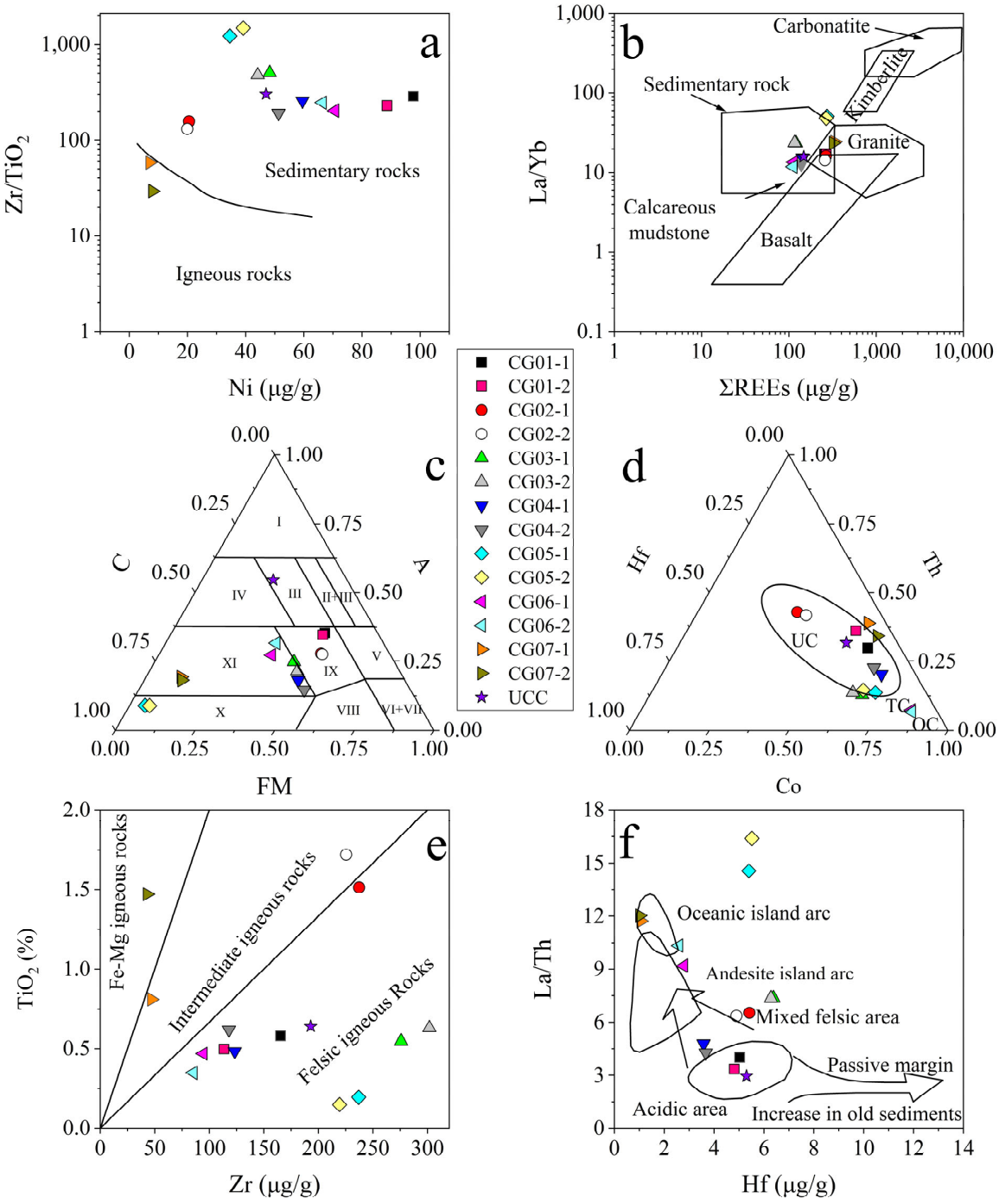


Figure 6. The restoration and nature of original rocks based on elemental analysis. (**a**) the Ni vs. Zr/TiO_2 plot, (**b**) the ∑REEs vs. La/Yb plot, (**c**) the FM-A-C plot, (**d**) the Co-Th-Hf plot, (**e**) the Zr vs. TiO_2 plot, and (**f**) the Hf vs. La/Th plot. In (**c**), A (aluminum coefficient) = $Al_2O_3/\Sigma \times 100$, C (calcium coefficient) = $CaO/\Sigma \times 100$, F (iron coefficient) = $(FeO + 2Fe_2O_3)/\Sigma \times 100$, M (magnesium coefficient) = $MgO/\Sigma \times 100$, $\Sigma = Al_2O_3 + CaO + FeO + 2Fe_2O_3 + MgO$, A + C + F + M = 100 [44]. Various oxides are calculated based on molecule number. I—muddy rock, II—clayey graywacke, III—volcanic rocks or greywacke, IV—arkose, V—tuffaceous siltstone, VI—ferrosilicon sedimentary rocks, VII + VIII—ultrabasic rock, IX—basic volcanic rock or dolomitic mudstone, X—calcium carbonate rock, XI—quartzite. In (**d**), UC—Upper Crust, TC—The Crust, OC—Oceanic Crust. There are same legends for (**a**–**f**).

As shown in Figure 6d, except for samples from CG06 plotting near the average continental crust (TC) value, all other samples fall within the upper crust field (UC). This indicates a predominant UC origin for the protoliths of these rock layers. In sedimentary rocks, an Al_2O_3/TiO_2 ratio < 14 typically suggests a mafic rock source, while the ratio between 19 and 28 points to a felsic derivation [47]. In this study, Al_2O_3/TiO_2 ratios for most samples exceed 14, while the ratios are less than 14 for samples from layers CG02 and CG07 (Table 1). Consequently, the protoliths of metamorphic rocks are originally linked to felsic rocks, while those in a few layers are associated with mafic rocks such as serpentinite. Chromium (Cr) is primarily hosted in chromite, while Zirconium (Zr) resides in zircon; thus, the Cr/Zr ratio can also be used to discriminate between felsic and mafic sources [48]. As listed in Table 1, Cr/Zr ratios in the metamorphic rocks change between 0.1 and 0.46, suggesting a felsic rock provenance. In the TiO_2 vs. Zr diagram (Figure 6e), all metamorphic rock samples except CG02-2 plot in the felsic rock field, but partly align with the result from the La/Th vs. Hf diagram, which can identify the protolith origin of different rock types (Figure 6f) [49]. Differing from sample CG02-1, sample CG02-2 plots in the intermediate igneous rock field, probably implying the CG02-2 protolith of intermediate igneous origin. Overall, the protoliths of metamorphic rocks in the Cheng-gang crystalline graphite deposit are primarily derived from upper-crustal felsic rocks.

6.2. Sedimentary Environments

Geochemical ratios may provide key indicators for reconstructing sedimentary environments. The Al/(Al + Fe + Mn) ratio serves as a proxy for evaluating hydrothermal sedimentation in marine sediments, with a value < 0.5 indicating hydrothermal input and a value > 0.5 showing terrigenous sedimentation [50]. Similarly, the Si/(Si + Al + Fe) ratio delineates a sedimentary environment, with the value between 0.9 and 1 indicating a bio-siliceous setting, whereas the value < 0.9 reflects a detrital provenance environment [51]. For paleo-salinity assessment of the sedimentary environment, a Sr/Ba ratio < 0.6 suggests brackish-water sedimentation, a value between 0.6 and 1 indicates saline water sedimentation, and a value > 1 reflects sedimentation under marine environments [52]. Redox conditions during rock formation may be inferred from multiple indices. A Th/U ratio > 7 points to an oxic environment, a value between 2 and 7 indicates a dysoxic environment, and a value < 2 shows an anaerobic environment [53–55]. Furthermore, an &U value > 1 indicates an anoxic reducing environment, while an &U value < 1 reflects an oxygenated oxic environment [44]. In addition, the V/(V + Ni) ratio reveals an oxygenated oxic environment when it is between 0.46 and 0.6, a suboxic/dysoxic transitional environment when it is between 0.6 and 0.84, and an anoxic reducing environment when it is higher than 0.84 [44].

As shown in Figure 7a, metamorphic rock samples could have their protolith formation in a terrigenous clastic, non-biosiliceous environment. Sr/Ba ratios of the metamorphic rocks vary from 0.15 to 0.69 (Table 1 and Figure 7b), reflecting that the protoliths formed in brackish-to-saline water facies predominantly of terrigenous origin. Th/U ratios of the metamorphic rocks range from 1.54 to 4.2, with a mean value of 2.72 (Table 1). As shown in Figure 7c, Th/U ratios are only slightly below 2 in CG04, indicating that the protolith formed in an anaerobic environment. In contrast, most of the metamorphic rocks have Th/U ratios between 2 and 7, suggesting that the protoliths formed in a dysoxic environment. As can be seen from Table 1, &U values are <1 in layers CG01 and CG05, but >1 in samples from other layers, indicating that the protoliths of these two layers formed in an oxygenated oxic environment, while other layers formed in an anoxic reducing environment. V/(V + Ni) ratios of the metamorphic rock samples all fall between 0.6 and 0.84, indicating that the protoliths formed in an anoxic environment (Figure 7d). In a word, these element ratios

confirm the hypothesis that the protoliths of the metamorphic rocks deposited under marine environments with low oxygen or a seasonal lack of oxygen [31].

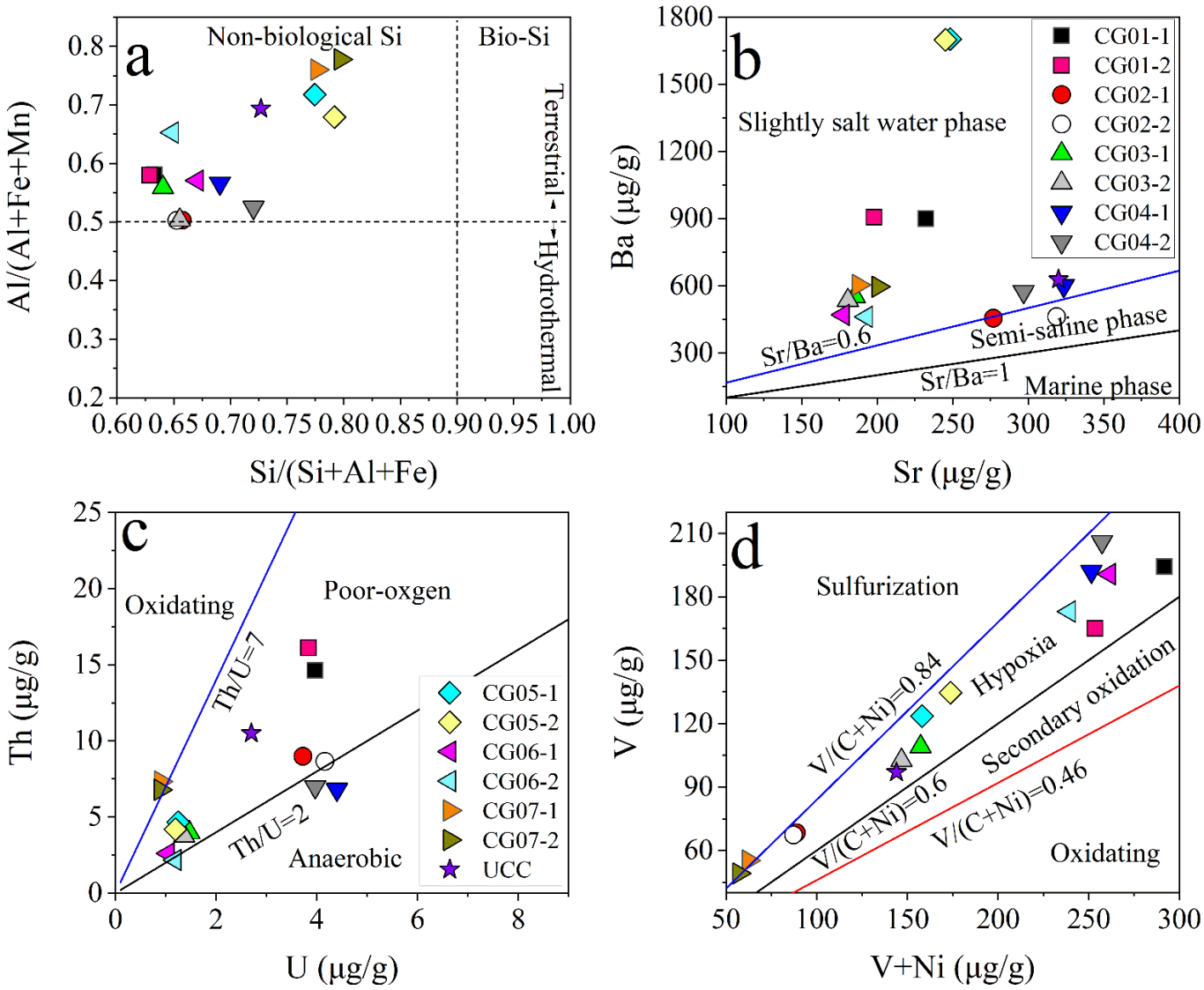


Figure 7. The diagrams of elemental ratios indicating palo-sedimentary environments of the Chenggang crystalline graphite deposit. (**a**) the plot of Si/(Si+Al+Fe) vs. Al/(Al+Fe+Mn), (**b**) the Sr vs. Ba plot, (**c**) the U vs. Th plot, and (**d**) the (V+Ni) vs. V plot. The UCC data are from reference [40]. The legends are the same for (**a**–**d**).

6.3. Carbonaceous Source

Stable carbon isotopes have proven to be a valuable tool for tracing carbon sources in graphite deposits [14,18,20,23,56]. There are usually three potential carbon sources showing different $\delta^{13}C$ values, namely, the values between −17‰ and −40‰ with an average of −27‰ for organic matter [57,58], the values around −2‰ to +4‰ with an average of 0‰ for marine carbonates [59], and the values near −7‰ for mantle-derived carbon [60]. The stable carbon isotopes and origin of graphite in graphite deposits have been widely investigated by authors, as shown in Figure 8. At present, two main hypotheses are proposed for graphite origin, that is, they are organic-matter- and inorganic-matter-derived [17,19,20,61,62].

The organic origin hypothesis points out that crystalline graphite forms through medium-to-high-grade regional metamorphism of organic carbon-rich sedimentary rocks.

The inorganic origin hypothesis attributes graphite formation to (i) crystallization from CO_2 released during marble formation via carbonate metamorphism, and/or (ii) redox-driven crystallization from carbon-bearing components (e.g., CO_2, CH_4) introduced by magmatic processes. Organic matter-derived graphite exhibits lighter stable carbon isotope composition, while inorganic matter-derived graphite has a wide range of stable carbon isotope ratios [56,63,64]. Most of the graphite deposits in China are mainly of organic origin, showing more negative $\delta^{13}C$ values (Figure 8). Graphite deposits in places such as Sri Lanka and Alpine Corsica are typically of inorganic origin [3,56,64], showing more positive $\delta^{13}C$ values (Figure 8). Graphite deposits in places such as Borrowdala, Huelma and Black Hills are also of inorganic origin but show lighter carbon isotope compositions [15,65,66] (Figure 8). This type of graphite deposit is strongly associated with C-O-H fluids, which assimilate carbon-bearing metapelites. The chemical reaction of inorganic carbon could also produce ^{12}C-enriched graphite in carbonate-bearing rocks, for example, thermal decomposition of Fe-carbonate, calcite reduction, and Fischer–Tropsch-type synthesis [11,64,67–71]. Therefore, graphite with depleted $\delta^{13}C$ values is not exclusively indicative of biogenic origin.

As shown in Figure 8, the $\delta^{13}C_{VPDB}$ value of graphite in the Cheng-gang crystalline graphite deposit crosses the organic and inorganic fields and is similar to those in places such as South China Craton (SCC), Tugeman and Southern India, but is significantly different from those in places such as Alpine Corsica, Tianshan and Sri Lanka [3,64,72–75]. This implies the genetic diversity of graphite within the Cheng-gang crystalline graphite deposit, that is, graphite in various rock layers, is different in origin.

In particular, samples from the granite layer (CG07) show the $\delta^{13}C_{VPDB}$ value of carbonate being within the isotope field of marine carbonate and having low fixed carbon contents (Figure 5 and Table S1). This result implies that magmatic intrusion did not trap organic matter-enriched sedimentary rocks. Therefore, the graphite ore did not form from magmatic fluids. Also, since magmatic intrusion was not observed in the overlying metamorphic rock layers, it was thus inferred that these metamorphic layers were not associated with magmatic fluids. In layers CG05 (olivine marble) and CG02 (tremolite–plagioclase gneiss), the $\delta^{13}C_{VPDB}$ values of carbonates also fall within the isotope field of marine carbonate and their fixed carbon contents are as low as below 1% (Figure 5 and Table S1). The significant difference lies in the carbonate content between the two layers (Figure 2). In theory, in layer CG05, the existence of enough carbonates should benefit ^{13}C- or ^{12}C-enriched graphite ore formation through decarbonation and/or other chemical reactions of inorganic carbon [64,66]. However, graphite ore did not form in the inorganic carbon-bearing layer. It is possible that inorganic carbon reactions did not occur because the graphite–magnetite association, wollastonite co-produced by calcite reduction, and the association of graphite with a catalyst for the Fischer–Tropsch-type (FTT) reaction (e.g., magnetite) were not observed in this layer [13]. Therefore, the activity of inorganic carbon-bearing metamorphic fluid did not drive the formation of graphite for layer CG05. Similarly, it is unlikely that this type of metamorphic fluid activity caused graphite ore formation in layer CG02 and graphite-ore-bearing gneiss layers CG01, CG03, CG04, and CG06, because these layers contain much less carbonate and there is no evidence of inorganic carbon chemical reactions (Figure 2).

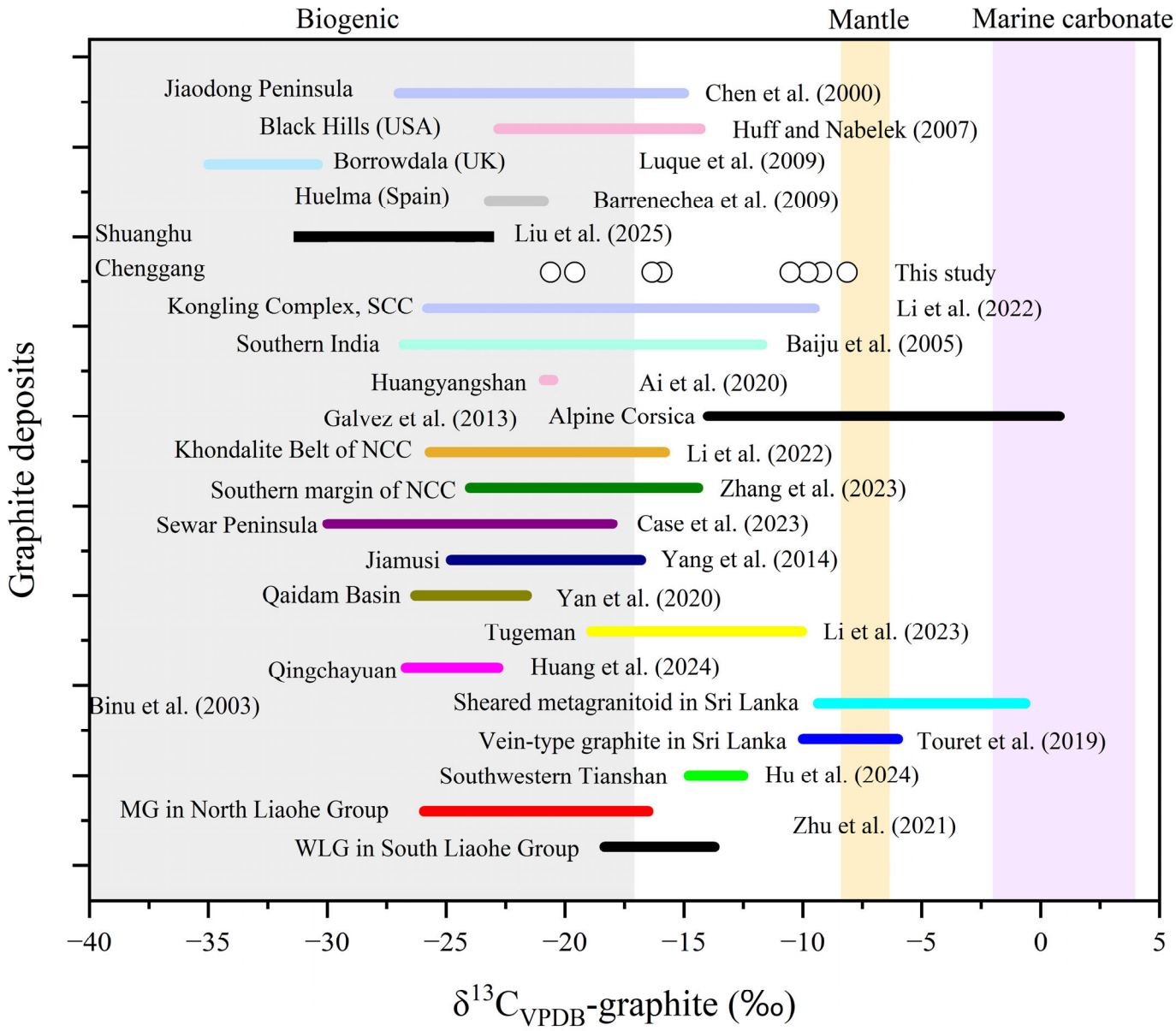


Figure 8. Stable carbon isotope comparison of graphite deposits worldwide. The carbon isotope data are from [18] for Jiaodong Peninsula, from [65] for Black Hills, from [66] for Borrowdala (UK), from [15] for Huelma (Spain), from [44] for Shuanghu, from this study for Chenggang, from [72] for Kongling Complex (SCC), from [73] for Southern India, from [76] for Huangyangshan, from [64] for Alpine Corsica, from [72] for Khondalite Belt of NCC, from [26] for Southern margin of NCC, from [7] for Sewar Peninsula, from [19] for Jiamusi, from [24] for Qaidam Basin, from [74] for Tugeman, from [23] for Qingchayuan, from [56] for sheared metagranitoid in Sri Lanka, from [3] for vein-type graphite in Sri Lanka, from [75] for Southwestern Tianshan, from [14] for MG in North Liaohe Group, from [14] for WLG in South Liaohe Group.

Regarding the graphite ore-bearing layers, if graphite was completely sourced from the transformation of sedimentary organic matter with a lighter carbon isotope composition under metamorphism, its $\delta^{13}C_{VPDB}$ value should be lower than that of organic matter [13,21]. The $\delta^{13}C_{VPDB}$ value of the graphite in layer CG01 definitely falls within the range of organic matter (Figure 5b), suggesting that the graphite is of organic origin. However, as shown in Figure 5b, the $\delta^{13}C_{VPDB}$ value of the graphite in layers CG03, CG04 and CG06 is actually higher than that of organic matter, showing that complete transformation of sedimentary organic matter was not the major mechanism controlling graphite ore formation. Two

possible explanations were already proposed by authors for the increasing trend of graphite $\delta^{13}C_{VPDB}$ [13,18,19]. One is a fluid-mixing model, which depicted the mixing of fluids from ^{12}C-enriched sources (outgassed during regional metamorphism of the sediments) with externally derived carbonic fluids rich in ^{13}C (likely from sub-lithospheric sources) through Rayleigh fractionation [18,19]. The origin of graphite with heavier carbon isotopes in quartz veins and leucosomes in the khondalite belt of the NCC was well-explained by this model [18,19]. Although this mechanism can explain the increasing trend of graphite $\delta^{13}C_{VPDB}$ values (Figure 5b), significant discrepancies that prevent this hypothesis from being fully accepted remain. No graphite veins occur in the study area and hand specimens, and the graphite deposit is distributed in the layered strata without fluid precipitation, similar to the study of Zhu et al. (2021) [14]. Therefore, the first explanation is not suitable for the carbon isotope of graphite in the Cheng-gang crystalline graphite deposit. The other possible explanation is that the residual organic carbon isotope gradually becomes heavier when the isotopically light CH_4 is degassed from the rock system since CH_4 is the main decomposition product of organic matter in a reducing environment [14,77]. Subsequently, the release of CH_4 due to organic matter decomposition could be trapped into inorganic fluids nearby during metamorphism, leading to the $\delta^{13}C_{VPDB}$ decrease in carbonates in graphite-ore-bearing layers. This explanation can agree well with the stable carbon isotope characteristics of graphite and carbonate in the Cheng-gang crystalline graphite deposit. As shown in Figure 5b, the variation in graphite $\delta^{13}C_{VPDB}$ value across graphite-ore-bearing layers reflects the difference in metamorphic temperatures [78], while the change in carbonate $\delta^{13}C_{VPDB}$ value across graphite-ore-bearing layers shows the difference in the CH_4-trapped ability of inorganic fluid [11]. Because carbonate minerals are not dominant in the graphite-ore-bearing layers (gneiss type), it is unclear whether inorganic fluid generated from surrounding marble rocks during metamorphism influenced the stable carbon isotope composition of graphite in the Cheng-gang crystalline graphite deposit through direct mixing. This possibility requires further in-depth investigation in future studies. In a word, the second explanation is accepted for graphite origin in this study.

Assuming the existence of isotope exchange between carbonate and graphite, the metamorphic temperature of the Cheng-gang crystalline graphite deposit can be evaluated using the following two formulas [78,79]

$$\Delta^{13}C_{Cal\text{-}Gr} = 5.81 \times 10^6 \times T^{-2}\,(K) - 2.61 \quad (3)$$

$$\Delta^{13}C_{Cal\text{-}Gr} = 5.6 \times 10^6 \times T^{-2}\,(K) - 2.4 \quad (4)$$

$\Delta^{13}C_{Cal\text{-}Gr}$ means the $\delta^{13}C$ difference between carbonate and graphite, T is Kelvin temperature with the unit K.

As listed in Table 2, the evaluated metamorphic temperature results based on the two methods mentioned above are similar for each rock layer. As a whole, the metamorphic temperature is distinct among graphite-ore-bearing layers. In particular, the metamorphic temperatures are as low as under 350 °C in layers CG01 and CG06, corresponding to the phase of greenschist facies, whereas layers CG03 and CG04 display metamorphic temperatures of 580–860 °C, corresponding to amphibolite–granulite facies during regional metamorphism [32,80]. For layers CG03 and CG04, the small $\Delta^{13}C_{Cal\text{-}Gr}$ values indicate isotope equilibrium between two mineral phases, and thus, the calculated temperature could represent peak metamorphism, while for layers CG01 and CG06, the large $\Delta^{13}C_{Cal\text{-}Gr}$ values show that either calcite or graphite did not attain isotopic equilibrium, or the pristine isotopic composition of minerals were also affected by external influences [10]. Advanced methods such as Raman spectroscopy analysis are required to corroborate the reliability of isotope-based metamorphic temperature in future studies.

Table 2. Metamorphic temperature of graphite in the Cheng-gang crystalline graphite deposit.

Sample	$\delta^{13}C_{VPDB}$-Graphite (‰)	$\delta^{13}C_{VPDB}$-Carbonate (‰)	$\Delta^{13}C_{Cal\text{-}Gr}$	Metamorphic Temperature (°C)	
				Wada et al. (1983) [78]	Dunn and Valley (1992) [79]
CG01-1	−19.59	−6.99	12.60	338	345
CG01-2	−20.61	−6.10	14.51	302	309
CG03-1	−8.13	−6.16	1.97	859	854
CG03-2	−9.21	−5.80	3.41	709	709
CG04-1	−9.77	−4.92	4.85	606	609
CG04-2	−10.53	−5.36	5.17	587	591
CG06-1	−15.92	−2.93	12.98	330	337
CG06-2	−16.34	−3.06	13.28	325	332

Note: Kelvin temperature (K) = Celsius temperature (°C) + 273.15.

7. Conclusions

In this study, mineralogical, elemental and isotopic characteristics of rock samples from various layers of borehole ZK8501 were investigated to elucidate the depositional environments and carbonaceous sources of the Cheng-gang crystalline graphite deposit within the Tan-Lu Fault Zone, yielding the following major findings:

(1) The fixed carbon content is higher (2%–3%) in the graphite-ore-bearing layers but is below 1% in the other rock layers. The gneiss host rocks consist of graphite, quartz, and plagioclase. The marble consists of calcite, olivine, and phlogopite, while the granite includes quartz, amphibole, and olivine. The graphite diffraction peaks (d002) show interlayer spacings of 3.3805 to 3.3811 Å, and the *r* values of 0.68488 to 0.69186 seem to indicate a high graphitization degree.

(2) The geochemical characteristics of various layers are different to some extent, depending on host-rock types, but overall show the enrichments of SiO_2, Ba, Zn, V, Zr, Pb, and LREEs. The metamorphic rocks are predominantly of the para-metamorphic type, and their protoliths consist of greywacke, clastic rocks, and carbonate rocks, and vary to certain degree with layers. In addition, their protoliths are primarily of upper-crustal felsic origin, and deposited under brackish environments with suboxic–anoxic conditions.

(3) The $\delta^{13}C_{VPDB}$ value of graphite in this deposit is higher than the average value of organic matter, while the $\delta^{13}C_{VPDB}$ values of carbonate is overall lower than the average value of marine carbonate in this deposit. The isotope fractionation mechanism responsible for the observed result is interpreted as follows: during metamorphism, the isotopically light CH_4 was progressively degassed from the rock system, causing the residual organic carbon to become isotopically heavier. The released CH_4 was subsequently trapped into adjacent inorganic fluids, leading to the $\delta^{13}C_{VPDB}$ decrease in carbonates in graphite-ore-bearing layers. Assuming the existence of isotope exchange between carbonate and graphite, peak metamorphism could happen at 580–860 °C.

The depositional environment and carbon sources of the Cheng-gang crystalline graphite deposit are well-clarified in this study. In future work, the uses of Raman spectroscopy and zircon geochronology are preferably considered for precisely determining the mineralization processes and mechanisms of graphite deposits in the Tan-Lu Fault Zone and guiding regional mineral exploration.

Supplementary Materials: The following supporting information can be downloaded at https://www.mdpi.com/article/10.3390/min16020120/s1, Table S1: Fixed carbon content (%), and the $\delta^{13}C_{VPDB}$ values (‰) of graphite and carbonate in rock samples from the Cheng-gang crystalline graphite deposit.

Author Contributions: Conceptualization, writing—original draft preparation, F.L. and W.R.; methodology, software, formal analysis, Y.Z. and J.C.; investigation, validation, Y.Z., F.L. and W.Y.; data curation, visualization, J.C.; supervision, W.R.; writing—review and editing, F.L., W.R. and J.C.; funding acquisition, project administration, W.Y. and J.C. All authors have read and agreed to the published version of the manuscript.

Funding: This research was funded by the Special Fund Projects for Natural Resources Development in Jiangsu Province (SCZH2021-46, SCZH2023-30), and the Deep Earth Probe and Mineral Resources Exploration-National Science and Technology Major Project (2024ZD1001000).

Data Availability Statement: The original contributions presented in the study are included within the article. Further inquiries can be directed to the corresponding author.

Acknowledgments: We would like to thank Sipu Ren and Ziling Xu for helping with sample pretreatment and experimental analysis. Lin Shi is also appreciated for helping with field sampling. The reviewers and editors are sincerely thanked for their valuable comments and suggestions.

Conflicts of Interest: The authors declare no conflicts of interest.

Appendix A

Table A1. The contents of elements in national geological reference materials (GBW07401-07408).

Sample	GBW07401	GBW07402	GBW07403	GBW07404	GBW07405	GBW07406	GBW07407	GBW07408
SiO_2 *	56.60 ± 0.46	65.97 ± 0.55	72.97 ± 0.40	63.33 ± 0.47	61.52 ± 0.39	45.35 ± 0.33	33.73 ± 0.35	60.12 ± 0.30
Al_2O_3 *	12.92 ± 0.21	11.70 ± 0.17	12.97 ± 0.14	16.93 ± 0.18	16.88 ± 0.15	26.63 ± 0.14	27.39 ± 0.50	11.81 ± 0.17
TFe_2O_3 *	4.41 ± 0.20	4.22 ± 0.14	2.63 ± 0.10	6.92 ± 0.15	9.80 ± 0.21	12.39 ± 0.17	18.03 ± 0.15	4.37 ± 0.14
MgO *	1.17 ± 0.04	1.40 ± 0.03	0.61 ± 0.02	1.33 ± 0.04	0.70 ± 0.02	0.20 ± 0.02	0.31 ± 0.02	2.00 ± 0.04
CaO *	2.78 ± 0.11	4.00 ± 0.14	0.84 ± 0.03	(0.13)	(0.07)	0.13 ± 0.02	(0.2)	7.59 ± 0.14
Na_2O *	1.65 ± 0.07	2.67 ± 0.06	2.54 ± 0.07	(0.1)	(0.1)	(0.14)	(0.1)	1.71 ± 0.06
K_2O *	2.85 ± 0.08	3.03 ± 0.08	2.91 ± 0.06	3.00 ± 0.07	2.14 ± 0.06	0.44 ± 0.02	0.35 ± 0.02	2.30 ± 0.05
MnO *	0.131 ± 0.006	0.092 ± 0.003	0.033 ± 0.001	0.030 ± 0.001	0.051 ± 0.002	0.23 ± 0.01	0.19 ± 0.01	0.063 ± 0.002
P_2O_5	0.23 ± 0.02 *	512 ± 30	0.042 ± 0.002 *	0.031 ± 0.003 *	353 ± 40	0.024 ± 0.004 *	0.21 ± 0.02 *	0.068 ± 0.003 *
TiO_2 *	0.326 ± 0.009	0.28 ± 0.02	0.228 ± 0.010	0.46 ± 0.02	0.61 ± 0.03	0.434 ± 0.019	2.06 ± 0.10	0.37 ± 0.02
LOI *	15.82 ± 0.64	5.87 ± 0.34	3.72 ± 0.27	(6.97)	7.22 ± 0.25	(13.22)	15.36 ± 0.92	8.98 ± 0.32
FeO *	(2.25)	(0.78)	(0.55)	(0.43)	(0.19)	(0.1)	(1.46)	1.23 ± 0.09
Li	28 ± 2	22 ± 1	18 ± 1	27 ± 2	51 ± 3	43 ± 2	23 ± 2	33 ± 2
Rb	137 ± 9	95 ± 4	85 ± 6	152 ± 5	142 ± 6	118 ± 13	28 ± 3	96 ± 5
Cs	7.2 ± 0.5	4.7 ± 0.3	3.2 ± 0.2	12.5 ± 0.9	18 ± 2	9.4 ± 0.8	2.9 ± 0.6	7.3 ± 0.5
Sr	192 ± 9	248 ± 6	325 ± 12	58 ± 2	39 ± 3	30 ± 4	37 ± 5	197 ± 6
Ba	700 ± 40	1187 ± 38	1117 ± 32	312 ± 15	343 ± 15	181 ± 21	237 ± 24	492 ± 17
Sc	8.3 ± 0.3	9.5 ± 0.5	5.6 ± 0.4	15.9 ± 0.6	16.9 ± 1.2	17 ± 2	25 ± 2	11.5 ± 0.6
V	61 ± 4	65 ± 5	45 ± 3	125 ± 6	136 ± 7	108 ± 5	240 ± 11	80 ± 3
Cr	44 ± 3	52 ± 4	35 ± 3	81 ± 4	113 ± 7	86 ± 8	379 ± 24	65 ± 4
Co	10.3 ± 0.6	11.1 ± 0.5	6.9 ± 0.6	20 ± 1	18 ± 2	20 ± 2	93 ± 4	12.3 ± 1.0
Ni	16.9 ± 1.5	24 ± 2	15 ± 1	36 ± 2	38 ± 2	75 ± 6	217 ± 8	30 ± 2
Cu	42 ± 5	20 ± 2	13.4 ± 1.1	43 ± 2	147 ± 10	358 ± 18	84 ± 7	24 ± 2
Zn	475 ± 30	58 ± 3	39 ± 3	92 ± 3	172 ± 7	1529 ± 79	187 ± 13	66 ± 3
Zr	218 ± 10	219 ± 13	247 ± 15	234 ± 5	272 ± 9	156 ± 5	370 ± 20	241 ± 6
Nb	15.3 ± 1.4	35 ± 4	10.6 ± 1.0	16.1 ± 1.2	20 ± 2	38 ± 3	80 ± 4	13.1 ± 1.2
Hf	6.5 ± 0.5	6.3 ± 0.5	7.1 ± 0.7	6.9 ± 0.7	8.3 ± 1.0	6.5 ± 1.0	8.9 ± 1.1	6.9 ± 0.8
Ta	1.3 ± 0.1	(0.86)	1.2 ± 0.2	1.4 ± 0.2	1.6 ± 0.3	16 ± 3	5.7 ± 0.9	1.1 ± 0.1
Pb	339 ± 12	27 ± 2	28 ± 2	37 ± 3	245 ± 14	478 ± 16	18.3 ± 2.1	21 ± 2
Th	13.1 ± 0.9	13.3 ± 0.9	6.7 ± 0.8	19 ± 2	17.2 ± 1.7	35 ± 6	10.5 ± 1.4	12.2 ± 0.9
U	6.0 ± 0.3	1.9 ± 0.2	1.2 ± 0.2	3.0 ± 0.3	4.0 ± 0.4	28 ± 2	2.6 ± 0.2	2.3 ± 0.3
Y	38 ± 3	25 ± 2	16 ± 2	23 ± 2	29 ± 2	33 ± 4	25 ± 3	26 ± 1
La	39 ± 2	61 ± 3	21 ± 3	54 ± 4	35 ± 3	31 ± 2	56 ± 6	35 ± 3
Ce	71 ± 5	123 ± 6	45 ± 4	99 ± 7	85 ± 5	85 ± 11	113 ± 13	68 ± 5
Pr	8.5 ± 0.7	14.8 ± 1.2	4.9 ± 0.4	11.2 ± 0.9	7.3 ± 0.6	5.6 ± 0.7	11.7 ± 1.7	8.0 ± 0.6
Nd	30.8 ± 1.3	55 ± 3	19 ± 2	40 ± 3	27 ± 3	20 ± 2	47 ± 5	31 ± 2
Sm	5.9 ± 0.4	7.9 ± 0.4	3.5 ± 0.2	6.8 ± 0.5	4.5 ± 0.3	4.7 ± 0.4	9.3 ± 1.1	6.0 ± 0.5
Eu	0.89 ± 0.08	1.8 ± 0.2	0.8 ± 0.2	1.2 ± 0.2	1.0 ± 0.2	0.39 ± 0.07	3.0 ± 0.5	1.2 ± 0.2
Gd	5.5 ± 0.4	6.2 ± 0.4	3.1 ± 0.3	5.5 ± 0.3	4.5 ± 0.6	4.2 ± 0.5	8.3 ± 0.6	5.5 ± 0.5
Tb	0.98 ± 0.09	0.89 ± 0.07	0.50 ± 0.04	0.84 ± 0.07	0.80 ± 0.07	0.84 ± 0.09	1.2 ± 0.2	0.86 ± 0.10
Dy	6.0 ± 0.5	4.5 ± 0.4	2.8 ± 0.3	4.4 ± 0.4	5.1 ± 0.4	5.4 ± 0.5	5.7 ± 0.5	4.9 ± 0.4
Ho	1.3 ± 0.2	0.9 ± 0.1	0.58 ± 0.06	0.85 ± 0.08	1.1 ± 0.2	1.1 ± 0.2	1.0 ± 0.2	0.98 ± 0.12
Er	3.8 ± 0.4	2.5 ± 0.4	1.7 ± 0.2	2.5 ± 0.3	3.2 ± 0.3	3.7 ± 0.5	2.4 ± 0.3	2.7 ± 0.3
Tm	0.61 ± 0.06	0.38 ± 0.03	0.28 ± 0.03	0.4 ± 0.1	0.50 ± 0.05	0.70 ± 0.09	0.33 ± 0.06	0.43 ± 0.04
Yb	3.8 ± 0.4	2.5 ± 0.3	1.8 ± 0.3	2.6 ± 0.3	3.2 ± 0.3	5.2 ± 0.6	2.0 ± 0.3	2.8 ± 0.3
Lu	0.57 ± 0.06	0.38 ± 0.04	0.28 ± 0.04	0.40 ± 0.07	0.49 ± 0.04	0.80 ± 0.11	0.30 ± 0.04	0.42 ± 0.04

Note: The unit is 10^{-2} for elements with * and 10^{-6} for elements without *. The values in brackets are suggested values.

Table A2. The contents of elements in national geological reference materials (GBW07301-073012).

Sample	GBW07301	GBW07302	GBW07303	GBW07304	GBW07305	GBW07306	GBW07307	GBW07308	GBW07309	GBW07310	GBW07311	GBW07312
SiO_2 *	59.07 ± 0.21	69.91 ± 0.17	71.29 ± 0.29	52.59 ± 0.26	56.44 ± 0.24	61.24 ± 0.13	64.70 ± 0.18	82.89 ± 0.27	64.89 ± 0.11	88.89 ± 0.19	76.25 ± 0.18	77.29 ± 0.13
Al_2O_3 *	15.36 ± 0.06	15.72 ± 0.10	12.04 ± 0.11	15.69 ± 0.13	15.37 ± 0.14	14.16 ± 0.09	13.41 ± 0.09	7.70 ± 0.09	10.58 ± 0.10	2.84 ± 0.07	10.37 ± 0.10	9.30 ± 0.11
TFe_2O_3 *	6.50 ± 0.15	1.90 ± 0.06	6.54 ± 0.09	5.91 ± 0.10	5.84 ± 0.09	5.88 ± 0.07	6.51 ± 0.09	2.20 ± 0.04	4.86 ± 0.07	3.86 ± 0.09	4.39 ± 0.07	4.88 ± 0.09
MgO *	3.30 ± 0.17	0.21 ± 0.02	0.68 ± 0.04	1.02 ± 0.04	0.98 ± 0.04	3.00 ± 0.06	3.08 ± 0.09	0.25 ± 0.02	2.39 ± 0.06	0.12 ± 0.04	0.62 ± 0.07	0.47 ± 0.08
CaO *	4.0 ± 0.1	0.25 ± 0.04	(0.22)	7.54 ± 0.12	5.34 ± 0.09	3.87 ± 0.07	1.67 ± 0.05	0.24 ± 0.04	5.35 ± 0.09	0.70 ± 0.03	0.47 ± 0.03	1.16 ± 0.05
Na_2O *	3.4 ± 0.1	3.03 ± 0.09	0.32 ± 0.03	0.30 ± 0.03	0.39 ± 0.03	2.30 ± 0.07	1.21 ± 0.04	0.47 ± 0.04	1.44 ± 0.04	0.039 ± 0.009	0.46 ± 0.03	0.44 ± 0.03
K_2O *	2.8 ± 0.1	5.20 ± 0.09	2.46 ± 0.06	2.23 ± 0.06	2.11 ± 0.07	2.43 ± 0.05	3.54 ± 0.08	2.84 ± 0.08	1.99 ± 0.06	0.125 ± 0.013	3.28 ± 0.07	2.91 ± 0.04
MnO	910 ± 28	240 ± 20	400 ± 23	825 ± 32	1160 ± 38	970 ± 37	690 ± 33	335 ± 16	620 ± 20	1010 ± 29	2490 ± 84	1400 ± 47
P_2O_5	1520 ± 77	200 ± 27	630 ± 39	470 ± 37	630 ± 25	1020 ± 42	820 ± 41	140 ± 22	670 ± 23	271 ± 15	255 ± 27	235 ± 22
TiO_2	5370 ± 210	1380 ± 80	6360 ± 230	5340 ± 160	5370 ± 160	4640 ± 120	4480 ± 120	3640 ± 110	5500 ± 160	1270 ± 70	2100 ± 100	1510 ± 50
LOI *	3.8 ± 0.3	-	-	-	-	-	-	-	7.21 ± 0.18	2.88 ± 0.12	(3.02)	2.62 ± 0.14
FeO *	(2.4)	0.56 ± 0.09	(0.72)	(0.91)	(0.94)	1.58 ± 0.14	1.50 ± 0.12	0.53 ± 0.09	1.53 ± 0.05	(0.26)	(0.35)	1.19 ± 0.07
Li	32 ± 3	101 ± 4	33 ± 1	51 ± 2	45 ± 2	40 ± 1	32 ± 1	13.2 ± 0.6	30 ± 1	13.0 ± 0.5	71 ± 2	39.0 ± 1.0
Rb	126 ± 7	470 ± 23	79 ± 6	130 ± 8	118 ± 6	107 ± 6	147 ± 8	132 ± 7	80 ± 3	9.2 ± 1.5	408 ± 11	270 ± 10
Cs	5.5 ± 0.2	16.6 ± 1.7	7.8 ± 0.7	10 ± 1	9.4 ± 0.9	9.1 ± 1.3	5.9 ± 0.7	3.6 ± 0.5	5.1 ± 0.8	2.3 ± 0.5	17.4 ± 0.8	7.9 ± 0.4
Sr	486 ± 32	(28)	90 ± 8	142 ± 12	204 ± 12	266 ± 18	220 ± 15	52 ± 6	166 ± 9	25 ± 3	29 ± 4	24 ± 3
Ba	920 ± 77	185 ± 24	615 ± 41	470 ± 37	440 ± 30	330 ± 24	720 ± 45	480 ± 32	430 ± 18	42 ± 7	260 ± 17	206 ± 15
Sc	14 ± 2	4.4 ± 0.7	14.3 ± 1.5	15.4 ± 1.7	14.5 ± 2.0	17 ± 2	14.6 ± 1.4	5.7 ± 0.4	11.1 ± 0.6	4.1 ± 0.4	7.4 ± 0.4	5.1 ± 0.4
V	115 ± 11	16.5 ± 1.9	120 ± 7	118 ± 6	109 ± 6	142 ± 8	96 ± 6	26 ± 3	97 ± 6	107 ± 5	47 ± 3	47 ± 4
Cr	128 ± 6	12 ± 3	87 ± 6	81 ± 6	70 ± 6	190 ± 15	122 ± 7	7.6 ± 1.4	85 ± 7	136 ± 10	40 ± 3	35 ± 3
Co	20 ± 2	2.6 ± 0.7	11.7 ± 1.1	18 ± 2	18.9 ± 2.1	24.4 ± 1.9	21 ± 2	3.6 ± 0.8	14.4 ± 1.2	15.3 ± 1.1	8.5 ± 0.8	8.8 ± 0.7
Ni	56 ± 7	5.5 ± 1.4	26 ± 3	40 ± 4	34 ± 3	78 ± 5	53 ± 4	(2.7)	32 ± 2	30 ± 2	14.3 ± 1.0	12.8 ± 1.3
Cu	28 ± 2	4.9 ± 0.5	177 ± 7	37 ± 2	137 ± 7	383 ± 12	38 ± 2	4.1 ± 0.5	32 ± 2	22.6 ± 1.3	79 ± 3	1230 ± 33
Zn	90 ± 7	44 ± 5	52 ± 4	101 ± 10	243 ± 15	144 ± 7	238 ± 12	43 ± 3	78 ± 4	46 ± 4	373 ± 14	498 ± 18
Zr	316 ± 16	460 ± 27	220 ± 14	188 ± 11	220 ± 11	170 ± 8	162 ± 9	490 ± 41	370 ± 20	70 ± 6	153 ± 13	234 ± 16
Nb	31.5 ± 1.9	95 ± 6	16 ± 2	18 ± 3	19 ± 3	12 ± 3	17 ± 2	35 ± 3	18 ± 2	6.8 ± 1.3	25 ± 3	15.4 ± 1.1
Hf	9.3 ± 0.7	20 ± 3	6.0 ± 1.9	5.8 ± 1.7	6.5 ± 1.9	4.9 ± 1.4	4.9 ± 1.4	14.5 ± 2.3	9.7 ± 1.5	1.8 ± 0.4	5.4 ± 0.6	8.3 ± 1.0
Ta	3.0 ± 0.3	15.3 ± 1.3	(1.0)	1.4 ± 0.2	1.4 ± 0.2	0.75 ± 0.09	1.35 ± 0.16	3.7 ± 0.7	1.3 ± 0.2	0.44 ± 0.12	5.7 ± 0.5	3.2 ± 0.3
Pb	3l ± 4	32 ± 5	40 ± 3	30 ± 5	112 ± 9	27 ± 4	350 ± 17	21 ± 3	23 ± 3	27 ± 2	636 ± 22	285 ± 1l
Th	27 ± 3	70 ± 4	9.2 ± 0.7	14.6 ± 1.0	15.2 ± 1.2	9.0 ± 1.4	12.6 ± 1.0	13.4 ± 0.8	12.4 ± 0.7	5.0 ± 0.3	23.3 ± 1.2	21.4 ± 1.1
U	4.6 ± 0.6	17 ± 2	1.9 ± 0.3	2.6 ± 0.4	2.6 ± 0.4	2.4 ± 0.4	3.5 ± 0.4	3.0 ± 0.2	2.6 ± 0.4	2.1 ± 0.2	9.1 ± 0.9	7.8 ± 0.7
Y	22 ± 2	67 ± 9	22 ± 3	26 ± 3	26 ± 3	20 ± 2	24 ± 2	18 ± 2	27 ± 2	14 ± 2	43 ± 5	29 ± 3
La	41 ± 2	90 ± 7	39 ± 5	40 ± 6	46 ± 5	39 ± 6	45 ± 5	30 ± 4	40 ± 3	13.0 ± 0.9	30 ± 2	32.7 ± 1.4
Ce	81 ± 7	192 ± 5	64 ± 5	78 ± 4	89 ± 7	68 ± 7	78 ± 6	54 ± 5	78 ± 6	38 ± 4	58 ± 4	61 ± 4
Pr	9.3 ± 0.9	18.6 ± 3.0	8.3 ± 1.1	9.3 ± 1.6	9.9 ± 1.3	8.4 ± 0.8	9.6 ± 1.5	5.8 ± 0.7	9.2 ± 0.8	3.2 ± 0.4	7.4 ± 0.5	6.9 ± 1.1
Nd	36 ± 3	62 ± 7	30 ± 4	32 ± 3	35 ± 4	33 ± 6	37 ± 5	2l ± 2	34 ± 2	11.8 ± 1.1	27 ± 2	26 ± 3

Table A2. *Cont.*

Sample	GBW07301	GBW07302	GBW07303	GBW07304	GBW07305	GBW07306	GBW07307	GBW07308	GBW07309	GBW07310	GBW07311	GBW07312
Sm	6.7 ± 0.4	10.8 ± 0.9	5.3 ± 0.4	6.2 ± 0.5	6.6 ± 0.5	5.6 ± 0.6	6.1 ± 0.5	3.8 ± 0.3	6.3 ± 0.4	2.4 ± 0.2	6.2 ± 0.3	5.0 ± 0.4
Eu	1.7 ± 0.2	0.49 ± 0.09	1.3 ± 0.1	1.31 ± 0.13	1.4 ± 0.3	1.50 ± 0.13	1.3 ± 0.2	0.56 ± 0.07	1.33 ± 0.06	0.47 ± 0.04	0.60 ± 0.06	0.61 ± 0.03
Gd	5.6 ± 0.6	9.5 ± 1.3	4.7 ± 0.3	5.0 ± 0.8	6.4 ± 1.1	5.5 ± 0.9	5.8 ± 0.8	3.5 ± 0.6	5.5 ± 0.4	2.2 ± 0.2	5.9 ± 0.4	4.4 ± 0.4
Tb	0.81 ± 0.07	1.8 ± 0.4	0.70 ± 0.09	0.90 ± 0.19	0.89 ± 0.19	0.69 ± 0.17	0.76 ± 0.16	0.54 ± 0.10	0.87 ± 0.09	0.42 ± 0.07	1.13 ± 0.09	0.82 ± 0.06
Dy	4.3 ± 0.3	11 ± 2	4.0 ± 0.5	4.6 ± 0.5	5.0 ± 0.5	3.8 ± 0.9	4.2 ± 0.6	2.6 ± 0.5	5.1 ± 0.3	2.2 ± 0.3	7.2 ± 0.6	4.8 ± 0.2
Ho	0.82 ± 0.11	2.6 ± 0.4	(0.9)	1.0 ± 0.2	0.95 ± 0.15	0.76 ± 0.10	0.96 ± 0.20	0.7 ± 0.2	0.96 ± 0.07	0.45 ± 0.07	1.4 ± 0.2	0.94 ± 0.07
Er	2.3 ± 0.4	8.2 ± 0.6	2.3 ± 0.4	2.5 ± 0.4	2.8 ± 0.5	2.2 ± 0.5	2.3 ± 0.3	1.8 ± 0.3	2.8 ± 0.3	1.3 ± 0.2	4.6 ± 0.5	3.1 ± 0.3
Tm	0.34 ± 0.04	1.55 ± 0.21	0.39 ± 0.08	0.46 ± 0.05	0.46 ± 0.07	0.35 ± 0.06	0.44 ± 0.12	0.33 ± 0.06	0.44 ± 0.07	0.20 ± 0.03	0.74 ± 0.09	0.53 ± 0.06
Yb	2.3 ± 0.2	11 ± 1	2.6 ± 0.2	2.9 ± 0.3	2.9 ± 0.3	2.1 ± 0.3	2.6 ± 0.3	2.1 ± 0.3	2.8 ± 0.3	1.2 ± 0.2	5.1 ± 0.6	3.7 ± 0.4
Lu	0.39 ± 0.04	(1.6)	0.39 ± 0.05	0.47 ± 0.14	0.46 ± 0.06	0.34 ± 0.09	0.39 ± 0.08	0.38 ± 0.07	0.45 ± 0.03	0.19 ± 0.03	0.78 ± 0.06	0.58 ± 0.06

Note: The unit is 10^{-2} for elements with * and 10^{-6} for elements without *. The values in brackets are suggested values.

Table A3. The contents of elements in national geological reference materials (GBW07103-07108).

Sample	GBW07103	GBW07104	GBW07105	GBW07106	GBW07107	GBW07108
SiO_2 *	72.83 ± 0.10	60.62 ± 0.14	44.64 ± 0.11	90.36 ± 0.15	59.23 ± 0.16	15.60 ± 0.06
Al_2O_3 *	13.40 ± 0.07	16.17 ± 0.12	13.83 ± 0.13	3.52 ± 0.09	18.82 ± 0.14	5.03 ± 0.08
TFe_2O_3 *	2.14 ± 0.06	4.90 ± 0.06	13.40 ± 0.19	3.22 ± 0.07	7.60 ± 0.09	2.52 ± 0.07
MgO *	0.42 ± 0.04	1.72 ± 0.06	7.77 ± 0.17	0.082 ± 0.020	2.01 ± 0.05	5.19 ± 0.12
CaO *	1.55 ± 0.05	5.20 ± 0.07	8.81 ± 0.09	0.30 ± 0.04	0.60 ± 0.04	35.67 ± 0.25
Na_2O *	3.13 ± 0.06	3.86 ± 0.07	3.38 ± 0.05	0.061 ± 0.014	0.35 ± 0.02	(0.08)
K_2O *	5.01 ± 0.07	1.89 ± 0.05	2.32 ± 0.06	0.65 ± 0.03	4.16 ± 0.10	0.78 ± 0.04
MnO	463 ± 18	604 ± 18	1310 ± 61	155 ± 7	173 ± 11	434 ± 27
P_2O_5	405 ± 20	1030 ± 24	4130 ± 122	970 ± 39	690 ± 34	226 ± 31
TiO_2	1720 ± 70	3090 ± 90	14200 ± 400	1580 ± 80	3950 ± 130	1960 ± 90
LOI *	(0.70)	4.44 ± 0.12	(2.24)	1.10 ± 0.07	(5.95)	34.1 ± 0.2
FeO *	1.02 ± 0.04	2.39 ± 0.07	7.60 ± 0.13	0.61 ± 0.05	1.39 ± 0.06	1.64 ± 0.06
Li	131 ± 5	18.3 ± 0.9	9.5 ± 0.9	11.1 ± 0.5	44 ± 2	20 ± 3
Rb	466 ± 17	38 ± 3	37 ± 4	29 ± 2	205 ± 8	32 ± 4
Cs	38.4 ± 1.2	2.3 ± 0.7	(0.7)	1.8 ± 0.3	14 ± 2	3.2 ± 0.7
Sr	106 ± 6	790 ± 35	1100 ± 64	58 ± 5	90 ± 7	913 ± 54
Ba	343 ± 29	1020 ± 45	527 ± 26	143 ± 14	450 ± 29	120 ± 12
Sc	6.1 ± 0.4	9.5 ± 0.7	15.2 ± 1.2	4.2 ± 0.3	18.5 ± 1.2	6.0 ± 1.1
V	24 ± 2	94 ± 4	167 ± 11	33 ± 3	87 ± 4	36 ± 6
Cr	3.6 ± 0.9	32 ± 3	134 ± 11	20 ± 3	99 ± 6	32 ± 6
Co	3.4 ± 0.7	13.2 ± 1.0	46.5 ± 3.4	6.4 ± 0.6	21 ± 2	9 ± 2
Ni	2.3 ± 0.8	17 ± 2	140 ± 7	16.6 ± 1.1	37 ± 3	18 ± 2
Cu	3.2 ± 0.9	55 ± 3	49 ± 3	19 ± 2	42 ± 2	23 ± 2
Zn	28 ± 3	71 ± 5	150 ± 10	20 ± 2	55 ± 4	52 ± 4
Zr	167 ± 9	99 ± 11	277 ± 20	214 ± 9	96 ± 9	62 ± 13
Nb	40 ± 3	6.8 ± 1.4	68 ± 8	5.9 ± 0.9	14.3 ± 1.6	6.6 ± 1.7
Hf	6.3 ± 0.8	2.9 ± 0.5	6.5 ± 0.8	6.6 ± 0.7	2.9 ± 0.5	1.8 ± 0.3
Ta	7.2 ± 0.7	0.40 ± 0.10	4.3 ± 0.6	0.38 ± 0.05	0.9 ± 0.1	0.42 ± 0.05
Pb	31 ± 3	11.3 ± 1.8	(7)	7.6 ± 0.8	8.7 ± 1.8	18 ± 3
Th	54 ± 3	2.6 ± 0.3	6.0 ± 0.8	7.0 ± 0.4	12.8 ± 0.9	4.1 ± 0.5
U	18.8 ± 1.4	0.90 ± 0.19	1.4 ± 0.3	2.1 ± 0.3	1.5 ± 0.3	1.9 ± 0.3
Y	62 ± 5	9.3 ± 1.2	22 ± 4	21.5 ± 2.2	26 ± 2	9.1 ± 1.6
La	54 ± 4	22 ± 2	56 ± 5	21 ± 2	62 ± 4	15 ± 4
Ce	108 ± 7	40 ± 3	105 ± 8	48 ± 4	109 ± 8	25 ± 3
Pr	12.7 ± 0.8	4.9 ± 0.4	13.2 ± 1.3	5.4 ± 0.6	13.6 ± 1.7	3.4 ± 0.4
Nd	47 ± 4	19 ± 2	54 ± 4	21 ± 2	48 ± 3	12.0 ± 1.0
Sm	9.7 ± 0.8	3.4 ± 0.2	10.2 ± 0.5	4.7 ± 0.3	8.4 ± 0.4	2.4 ± 0.2
Eu	0.85 ± 0.07	1.02 ± 0.05	3.2 ± 0.2	1.02 ± 0.08	1.7 ± 0.2	0.51 ± 0.05
Gd	9.3 ± 0.7	2.7 ± 0.4	8.5 ± 0.6	4.5 ± 0.4	6.7 ± 0.5	1.9 ± 0.2
Tb	1.65 ± 0.09	0.41 ± 0.05	1.2 ± 0.2	0.79 ± 0.09	1.02 ± 0.08	0.35 ± 0.05
Dy	10.2 ± 0.4	1.85 ± 0.17	5.6 ± 0.3	4.1 ± 0.4	5.1 ± 0.4	1.6 ± 0.2
Ho	2.05 ± 0.17	0.34 ± 0.03	0.88 ± 0.04	0.75 ± 0.12	0.98 ± 0.05	0.33 ± 0.05
Er	6.5 ± 0.3	0.85 ± 0.13	2.0 ± 0.2	2.0 ± 0.3	2.7 ± 0.4	1.0 ± 0.2
Tm	1.06 ± 0.09	0.15 ± 0.05	0.28 ± 0.04	0.32 ± 0.04	0.43 ± 0.03	0.17 ± 0.04
Yb	7.4 ± 0.5	0.89 ± 0.13	1.5 ± 0.4	1.9 ± 0.2	2.6 ± 0.3	0.90 ± 0.11
Lu	1.15 ± 0.09	0.12 ± 0.03	0.19 ± 0.05	0.30 ± 0.03	0.41 ± 0.05	0.14 ± 0.03

Note: The unit is 10^{-2} for elements with * and 10^{-6} for elements without *. The values in brackets are suggested values.

References

1. Luque, F.; Huizenga, J.; Crespo-Feo, E.; Wada, H.; Ortega, L.; Barrenechea, J. Vein graphite deposits: Geological settings, origin, and economic significance. *Miner. Depos.* **2014**, *49*, 261–277. [CrossRef]
2. Nassar, N.; Fortier, S. Methodology and technical input for the 2021 review and revision of the U.S. *Crit. Miner. List. Rep.* **2021**, *1045*, 31.

3. Touret, J.L.R.; Huizenga, J.M.; Kehelpannala, K.V.W.; Piccoli, F. Vein type graphite deposits in Sri Lanka: The ultimate fate of granulite fluids. *Chem. Geol.* **2019**, *508*, 167–181. [CrossRef]
4. Buseck, P.R.; Beyssac, O. From Organic Matter to Graphite: Graphitization. *Elements* **2014**, *10*, 421–426. [CrossRef]
5. Beyssac, O.; Rumble, D. Graphitic carbon: A ubiquitous, diverse, and useful geomaterial. *Elements* **2014**, *10*, 415–420. [CrossRef]
6. Yang, M.J.; Di, Y.J.; Zhang, D.; Wu, D.T.; Fang, Y.; Zhang, X.M. A new insight into the genesis of graphite deposits in Madagascar using U-Pb zircon dating and electron microprobe analysis. *Minerals* **2024**, *14*, 484. [CrossRef]
7. Case, G.N.D.; Karl, S.M.; Regan, S.P.; Johnson, C.A.; Ellison, E.T.; Caine, J.S.; Holm-Denoma, C.S.; Pianowski, L.S.; Marsh, J.H. Insights into the metamorphic history and origin of flake graphite mineralization at the Graphite Creek graphite deposit, Seward Peninsula, Alaska, USA. *Miner. Depos.* **2023**, *5*, 939–962. [CrossRef]
8. Santoro, L.; Bertone, V.; Ferrando, S.; Groppo, C. New insights into graphite deposits in Chisone and Germanasca Valleys (For a-Maira Massif, Western Italian Alps): Scientific advances and applied perspectives. *Minerals* **2025**, *15*, 455. [CrossRef]
9. Storetvedt, K.M.; Michaelsen, P. Sedimentary basins, hydrocarbons, graphite, coal, and Cu-Au deposits—From Mongolia to the Pacific margin: Interplay between the ubiquitous orthogonal fracture network and global wrench tectonics. *Mong. Geosci.* **2024**, *29*, 19–54. [CrossRef]
10. Sanyal, P.; Acharya, B.C.; Bhattacharya, S.K.; Sarkar, A.; Agrawal, S.; Bera, M.K. Origin of graphite, and temperature of metamorphism in Precambrian eastern Ghats Mobile Belt, Orissa, India: A carbon isotope approach. *J. Asian Earth Sci.* **2009**, *36*, 252–260. [CrossRef]
11. Luque, F.J.; Crespo-Feo, E.; Barrenechea, J.F.; Ortega, L. Carbon isotopes of graphite: Implications on fluid history. *Geosci. Front.* **2012**, *3*, 197–207. [CrossRef]
12. Li, C.; Wang, C.H.; Zhao, H.; Pei, H.X.; Li, X.W.; Zhou, L.M.; Du, A.D.; Qu, W.J. Minerogenetic regularity of graphite deposits in China. *Miner. Depos.* **2015**, *34*, 1223–1236, (In Chinese with English Abstract).
13. Guo, Z.X.; Papineau, D.; O'Neil, J.; Rizo, H.; Chen, Z.Q.; Qiu, X.C.; She, Z. Abiotic synthesis of graphitic carbons in the Eoarchean Saglek-Hebron metasedimentary rocks. *Nat. Commun.* **2024**, *15*, 5679. [CrossRef] [PubMed]
14. Zhu, J.J.; Liu, F.L.; Wang, F.; Xu, W.T.; Liu, F.X.; Shi, C. Carbon isotope and geochemical characteristics of the Paleoproterozoic graphite deposits in the Jiao-Liao-Ji belt, North China Craton: Implications for genesis and depositional environment. *Precambrian Res.* **2021**, *362*, 106320. [CrossRef]
15. Barrenechea, J.F.; Luque, F.J.; Millward, D.; Ortega, L.; Beyssac, O.; Rodas, M. Graphite morphologies from the Borrowdale deposit (NW England, UK): Raman and SIMS data. *Contrib. Min. Petrol.* **2009**, *158*, 37–51. [CrossRef]
16. Maibam, B.; Sanyal, P.; Bhattacharya, S. Geochronological study of metasediments and carbon isotopes in associated graphites from the Sargur area, Dharwar craton: Constraints on the age and nature of the protoliths. *J. Geol. Soc. India* **2015**, *85*, 577–585. [CrossRef]
17. Sun, X.H.; Ren, Y.S.; Sun, Z.J.; Wang, C.Y.; Li, Z.W. Geochronology and geochemical properties of the large-scale graphite mineralization associated with the Huangyangshan alkaline pluton, Eastern Junggar, Xinjiang, NW China. *Geochemistry* **2021**, *81*, 125820. [CrossRef]
18. Chen, Y.J.; Liu, C.Q.; Chen, H.Y.; Zhang, Z.J.; Li, C. Carbon isotope geochemistry of graphite deposits and ore-bearing khondalite series in North China: Implication for several geoscientific problems. *Acta Petrol. Sin.* **2000**, *16*, 233–244, (In Chinese with English Abstract).
19. Yang, Q.Y.; Santosh, M.; Wada, H. Graphite mineralization in Paleoproterozoic khondalites of the North China Craton: A carbon isotope study. *Precambrian Res.* **2014**, *255*, 641–652. [CrossRef]
20. Cui, N.; Sun, L.; Bagas, L.; Xiao, K.Y.; Xia, J.S. Geological characteristics and analysis of known and undiscovered graphite resources of China. *Ore Geol. Rev.* **2017**, *91*, 1119–1129. [CrossRef]
21. Zhong, Y.; Ma, X.D.; Li, H.K.; Zhai, M.G. Revisit and comparative analysis of the typical graphite deposits in the Paleoproterozoic khondalite series, western North China Craton: Implications for genesis, depositional environment and prospecting Potential. *Ore Geol. Rev.* **2019**, *109*, 370–380. [CrossRef]
22. Sun, L.; Xu, C.P.; Xiao, K.Y.; Zhu, Y.S.; Yan, L.Y. Geological characteristics, metallogenic regularities and the exploration of graphite deposits in China. *China Geol.* **2018**, *3*, 425–434. [CrossRef]
23. Huang, Y.; Jiao, W.W.; Liu, L.; Chen, J.J.; Ma, Y. Genesis of the Qingchayuan flake graphite deposit in the Huangling Dome of Yangtze Block, South China. *Minerals* **2024**, *14*, 1103. [CrossRef]
24. Yan, M.Q.; Zhang, D.H.; Huizenga, J.M.; Wei, J.H.; Li, H.; Li, G.M.; Huang, X.K.; Zhang, X.M.; Zhao, S.Q. Mineralogical and isotopic characterization of graphite deposits in the western part of the North Qaidam Orogen and East Kunlun Orogen, northeast Tibetan Plateau, China. *Ore Geol. Rev.* **2020**, *126*, 103788. [CrossRef]
25. Wang, J.Y.; Liu, J.C.; Zhang, H.D.; Zhang, H.D.; Zhang, H.R.; Li, Y. Metamorphism, geochemistry, and carbon source on sedimentary-metamorphic graphite deposits in eastern Shangdong, China. *Geol. J.* **2020**, *55*, 3748–3769. [CrossRef]

26. Zhang, C.; He, X.F.; Sun, L.X.; Santosh, M.; Chi, J.; Yu, X.Y.; Li, Z.S. Graphitization in Paleoproterozoic granulites from the Taihua Complex, North China Craton: Constraints from laser Raman spectroscopy, carbon isotopes and geochronology. *Lithos* **2023**, 454–455, 107266. [CrossRef]
27. Ma, Y.; Huang, Y.; Liu, L. Genesis of the Tianping flake graphite deposit at the western margin of Yangtze Block, SW China. *Ore Geol. Rev.* **2021**, *139*, 104434. [CrossRef]
28. Chen, P.J. Age and framework of layertal displacement of the Tanlu Fault. *Chin. Sci. Bull.* **1989**, *34*, 482–487.
29. Zhu, G.; Wang, Y.; Liu, G.; Wang, Y.; Li, C. $^{40}Ar/^{39}Ar$ dating of strike-slip motion on the Tan-Lu fault zone, East China. *J. Struct. Geol.* **2005**, *27*, 1379–1398. [CrossRef]
30. Shi, Y.R.; Kang, Y.L.; Peng, W.X. The Tanlu Fault: The largest lithospheric fault in eastern China. *Acta Geol. Sin.* **2025**, *99*, 104–119. (In Chinese with English Abstract)
31. Yao, W.J.; Zhang, Y.Y.; Shi, L.; Liu, F.; Shen, R.; Zhang, X. Geological characteristics and prospecting indicators of the Cheng-gang graphite deposit in Xinyi, Jiangsu. *China Non-Met. Miner. Indus.* **2024**, *3*, 31–35. (In Chinese with English Abstract)
32. Wang, W.; Song, C.Z.; Ren, S.L.; Li, J.H.; Zhang, Y.; Wang, P.P.; Hu, D. P-T condition and zircon U-Pb analysis of the Taoyuan ductile shear zone in Tan-Lu Fault. *Acta Petrol. Sin.* **2016**, *32*, 787–803. (In Chinese with English Abstract)
33. Zhao, T.; Zhu, G.; Lin, S.Z.; Wang, H.Q. Indentation-induced tearing of a subducting continent: Evidence from the Tan–Lu Fault Zone, East China. *Earth Sci. Rev.* **2016**, *152*, 14–36. [CrossRef]
34. Xu, J.W.; Zhu, G. Tectonic models of the Tanlu Fault Zone, Eastern China. *Int. Geol. Rev.* **1994**, *36*, 771–784. [CrossRef]
35. Kang, Y.L.; Shi, Y.R.; Anderson, J.L. Tectonic mechanism and evolution of eastern China during the Early Cretaceous: A view from magmatism in the middle to Southern Tan-Lu Fault Zone. *Int. Geol. Rev.* **2021**, *63*, 21–46. [CrossRef]
36. Zhu, G.; Wang, W.; Gu, C.C.; Zhang, S.; Liu, C. Late Mesozoic evolution history of the Tan-Lu Fault Zone and its indication to destruction processes of the North China Craton. *Acta Petrol. Sin.* **2016**, *32*, 935–949. (In Chinese with English Abstract)
37. Cao, X.L.; Lv, S.; Xu, K.; Wang, X.H.; Wang, J.X.; Liu, B.; Shen, K. Fabrication of matrix graphite with a high degree of graphitization for spherical fuel elements by using natural microcrystalline graphite fillers. *Nucl. Eng. Technol.* **2024**, *56*, 4851–4858. [CrossRef]
38. Hoefs, J. *Stable Isotope Geochemistry*; Springer: Berlin/Heidelberg, Germany, 2009; pp. 1–107.
39. Kwiecińska, B.; Petersen, H.I. Graphite, semi-graphite, natural coke, and natural char, classification—ICCP system. *Int. J. Coal Geol.* **2004**, *57*, 99–116.
40. Rudnick, R.L.; Gao, S. Composition of the continental crust. In *The Crust*; Rudnick, R.L., Ed.; Elsevier: Oxford, UK, 2003; Volume 3, pp. 1–64.
41. Taylor, S.R.; McLennan, S.M. *The Continental Crust: Its Composition and Evolution*; Blackwell: Oxford, UK, 1985; pp. 1–312.
42. McDonough, W.F.; Sun, S.S. The composition of the Earth. *Chem. Geol.* **1995**, *120*, 223–253. [CrossRef]
43. Wang, R.M.; He, G.P.; Chen, Z.Z.; Zheng, S.Y.; Gen, Y.S. *Graphic Discrimination of Metamorphic Rocks*; Geological Press: Beijing, China, 1987; pp. 1–199. (In Chinese)
44. Liu, F.; Rao, W.B.; Zhang, Y.Y.; Yao, W.J.; Shi, L.; Xu, M.Z.; Ren, S.P.; Li, X.H.; Li, Z.Y. Geochemical characteristics of the Shuanghu crystalline graphite deposit in East China: Implications for original rocks, sedimentary environments and carbon sources. *Front. Earth Sci.* **2025**, *13*, 1576709. [CrossRef]
45. Wincherter, J.A.; Park, R.G.; Holland, J.G. The geochemistry of Lewisian semipelitic schists from the Gairloch distric, Wester Ross. *Scot. J. Geol.* **1980**, *16*, 165–179. [CrossRef]
46. Simonen, A. Stratigraphy and sedimentation of the Svecofennidie, early Archean supracrustal rocks in southwestern Finland. *Bull. Geol. Soc. Finl.* **1953**, *160*, 1–64.
47. Girty, G.H.; Ridge, D.; Knaack, C.; Johnson, D.; AlRiyami, R.K. Provenance and depositional setting of Paleozoic chert and argillite, Sierra Nevada, California. *J. Sediment. Res.* **1996**, *66*, 107–118. [CrossRef]
48. Wronkiewicz, D.J.; Condie, K.C. Geochemistry and provenance of sediments from the Pongola Supergroup, South Africa: Evidence for a 3.0-Ga-old continental craton. *Geochim. Cosmochim. Acta* **1989**, *53*, 1537–1549.
49. Floyd, P.A.; Leveridge, B.E. Tectonic environment of the Devonian Gramscatho basin, south Cornwall: Framework mode and geochemical evidence from turbiditic sandstones. *J. Geol. Soc.* **1987**, *144*, 531–542. [CrossRef]
50. Boström, K.; Kraemer, T.; Gartner, S. Provenance and accumulation rates of opaline silica, Al, Ti, Fe, Mn, Cu, Ni and Co in Pacific pelagic sediments. *Chem. Geol.* **1973**, *11*, 123–148. [CrossRef]
51. Aitchison, J.C.; Flood, P.G. Geochemical constraints on the depositional setting of Palaeozoic cherts from the New England orogen, NSW, eastern Australia. *Mar. Geol.* **1990**, *94*, 79–95. [CrossRef]
52. Chivas, A.R.; de Deckker, P.; Shelley, J.M.G. Strontium content of ostracods indicates lacustrine palaeosalinity. *Nature* **1985**, *316*, 251–253. [CrossRef]

53. Hatch, J.R.; Leventhal, J.S. Relationship between inferred redox potential of the depositional environment and geochemistry of the Upper Pennsylvanian (Missourian) Stark Shale Member of the Dennis Limestone, Wabaunsee County, Kansas, USA. *Chem. Geol.* **1992**, *99*, 65–82. [CrossRef]
54. Jones, B.; Manning, D. Comparison of geochemical indices used for the interpretation of palaeoredox conditions in ancient mudstones. *Chem. Geol.* **1994**, *111*, 111–129. [CrossRef]
55. Adams, J.A.S.; Weaver, C.E. Thorium to uranium ratios as indications of sedimentary processes: Example of concept of geochemical facies. *AAPA Bull.* **1958**, *42*, 387–430.
56. Binu, L.S.S.; Kehelpannala, K.V.W.; Satish, K.M.; Wada, H. Multistage graphite precipitation through protracted fluid flow in sheared metagranitoid, Digana, Sri Lanka: Evidence from stable isotopes. *Chem. Geol.* **2003**, *197*, 253–270. [CrossRef]
57. Schidlowski, M. Carbon isotopes as biogeochemical recorders of life over 3.8 Ga of Earth history: Evolution of a concept. *Precambrian Res.* **2001**, *106*, 117–134. [CrossRef]
58. Sharp, Z. *Principles of Stable Isotope Geochemistry*; Pearson Prentice Hall: Upper Saddle River, NJ, USA, 2007; pp. 1–344.
59. Weis, P.L.; Friedman, I.; Gleason, J.P. The origin of epigenetic graphite: Evidence from isotopes. *Geochim. Cosmochim. Acta* **1981**, *45*, 2325–2332. [CrossRef]
60. Radhika, U.P.; Santosh, M.; Wada, H. Graphite occurrences in southern Kerala: Characteristics and genesis. *J. Geol. Soc. India* **1995**, *45*, 653–666. [CrossRef]
61. Santosh, M.; Wada, H. Microscale isotopic zonation in graphite crystals: Evidence for channeled CO_2 influx in granulite. *Earth Planet. Sci. Lett.* **1993**, *119*, 19–26. [CrossRef]
62. Duke, E.F.; Rumble, I.D. Textural and isotopic variations in graphite from plutonic rocks, South Central New Hampshire. *Contrib. Mineral. Petrol.* **1986**, *93*, 409–419. [CrossRef]
63. Zhang, C.; Santosh, M. Coupled laser Raman spectroscopy and carbon stable isotopes of graphite from the khondalite belt of Kerala, southern India. *Lithos* **2019**, *334–335*, 245–253. [CrossRef]
64. Galvez, M.E.; Beyssac, O.; Martinez, I.; Benzerara, K.; Chaduteau, C.; Malvoisin, B.; Malavieille, J. Graphite formation by carbonate reduction during subduction. *Nat. Geosci.* **2013**, *6*, 473–477. [CrossRef]
65. Huff, T.A.; Nabelek, P.I. Production of carbonic fluids during metamorphism of graphitic pelites in a collisional orogendan assessment from fluid inclusions. *Geochim. Cosmochim. Acta* **2007**, *71*, 4997–5017. [CrossRef]
66. Luque, F.J.; Ortega, L.; Barrenechea, J.F.; Millward, D.; Beyssac, O.; Huizenga, J.M. Deposition of highly crystalline graphite from moderate-temperature fluids. *Geology* **2009**, *37*, 275–278. [CrossRef]
67. McCollum, T.M.; Seewald, J.S. Carbon isotope composition of organic compounds produced by abiotic synthesis under hydrothermal conditions. *Earth Planet. Sci. Lett.* **2006**, *243*, 74–84. [CrossRef]
68. Runge, E.A.; Mansor, M.; Kappler, A.; Duda, J.P. Microbial biosignatures in ancient deep-sea hydrothermal sulfides. *Geobiology* **2023**, *21*, 355–377. [CrossRef] [PubMed]
69. Rumble, D. Hydrothermal graphitic carbon. *Elements* **2014**, *10*, 427–433. [CrossRef]
70. McCollom, T.M. Laboratory simulations of abiotic hydrocarbon formation in earth's deep subsurface. *Rev. Mineral. Geochem.* **2013**, *75*, 467–494. [CrossRef]
71. Dodd, M.S.; Papineau, D.; She, Z.B.; Manikyamba, C.; Wan, Y.S.; O'Neil, J.; Karhu, J.A.; Rizo, H.; Pirajno, F. Widespread occurrences of variably crystalline ^{13}C-depleted graphitic carbon in banded iron formations. *Earth Planet. Sci. Lett.* **2019**, *512*, 163–174. [CrossRef]
72. Li, Y.; Satish-Kumar, M.; Kiran, S.; Wan, C.; Zheng, J.P. 2.0 Ga orogenic graphite deposits and associated ^{13}C-enriched metacarbonate rocks from South China Craton: Implications for global lomagundi event. *Geosci. Front.* **2022**, *13*, 101409. [CrossRef]
73. Baiju, K.R.; Satish-Kumar, M.; Kagi, H.; Nambiar, C.G.; Ravisankar, M. Mineralogical Characterization of Graphite Deposits from Thodupuzha-Kanjirappally Belt, Madurai Granulite Block, Southern India. *Gondwana Res.* **2005**, *8*, 223–230. [CrossRef]
74. Li, H.; Hong, T.; Liu, S.K.; Ke, Q.; Yang, Z.Q.; Ma, Y.C.; Wang, X.H.; Niu, L.N.; Kang, K.; Xu, X.W. Genesis of the graphite from the Tugeman graphite deposit, Xinjiang, China: Evidence for carbon isotope refining by fluids associated with the ductile shear zone. *Minerals* **2023**, *12*, 1328. [CrossRef]
75. Hu, H.; Zhang, L.F.; Bader, T.; Huizenga, J.M.; Peng, W.G.; Lan, C.Y.; Liu, Y.Y. Fluid-deposited graphite in metapelites from the southwestern Tianshan orogen (China): Implications for carbon cycling in subduction zones. *Lithos* **2024**, *482–483*, 107733. [CrossRef]
76. Ai, J.; Lu, X.B.; Li, Z.W.; Wu, Y.L. Genesis of the graphite orbicules in the Huangyangshan graphite deposit, Xinjiang, China: Evidence from geochemical, isotopic and fluid inclusion data. *Ore Geol. Rev.* **2020**, *122*, 103505. [CrossRef]
77. Rumble, D.; Hoering, T.C. Carbon isotope geochemistry of graphite vein deposits from New Hamsphire, U.S.A. *Geochim. Cosmochim. Acta* **1986**, *50*, 1239–1247. [CrossRef]
78. Wada, H.; Suzuki, K. Carbon isotopic thermometry calibrated by dolomite-calcite solvus temperatures. *Geochim. Cosmochim. Acta* **1983**, *47*, 697–706. [CrossRef]

79. Dunn, S.; Valley, J. Calcite–graphite isotope thermometry: A test for polymetamorphism in marble, Tudor gabbro aureole, Ontario, Canada. *J. Metamorph. Geol.* **1992**, *10*, 487–501. [CrossRef]
80. Zhao, G.C.; Cawood, P.A.; Li, S.Z.; Wilde, S.A.; Sun, M.; Zhang, J.; He, Y.H.; Yin, C.Q. Amalgamation of the North China Craton: Key issues and discussion. *Precambrian Res.* **2012**, *222–223*, 55–76. [CrossRef]

Disclaimer/Publisher's Note: The statements, opinions and data contained in all publications are solely those of the individual author(s) and contributor(s) and not of MDPI and/or the editor(s). MDPI and/or the editor(s) disclaim responsibility for any injury to people or property resulting from any ideas, methods, instructions or products referred to in the content.